

# *Intraseasonal variability of air-sea fluxes over the Bay of Bengal during the southwest monsoon*

Article

Accepted Version

Sanchez-Franks, A., Kent, E. C., Matthews, A. J., Webber, B. G. M., Peatman, S. C. and Vinayachandran, P. N. (2018) Intraseasonal variability of air-sea fluxes over the Bay of Bengal during the southwest monsoon. *Journal of Climate*, 31 (17). pp. 7087-7109. ISSN 1520-0442 doi: 10.1175/JCLI-D-17-0652.1 Available at <https://centaur.reading.ac.uk/77492/>

It is advisable to refer to the publisher's version if you intend to cite from the work. See [Guidance on citing](#).

To link to this article DOI: <http://dx.doi.org/10.1175/JCLI-D-17-0652.1>

Publisher: American Meteorological Society

All outputs in CentAUR are protected by Intellectual Property Rights law, including copyright law. Copyright and IPR is retained by the creators or other copyright holders. Terms and conditions for use of this material are defined in the [End User Agreement](#).

[www.reading.ac.uk/centaur](http://www.reading.ac.uk/centaur)

**CentAUR**

Central Archive at the University of Reading

Reading's research outputs online

**Intraseasonal Variability of Air-Sea Fluxes over the Bay of Bengal during  
the Southwest Monsoon**

Alejandra Sanchez-Franks\*, Elizabeth C. Kent

*National Oceanography Centre, Southampton, UK*

Adrian J. Matthews, Benjamin G. M. Webber

*Centre for Ocean and Atmospheric Sciences, School of Environmental Sciences, University of  
East Anglia, Norwich, UK*

Simon C. Peatman

*National Centre for Atmospheric Science - Climate, University of Reading, UK*

P. N. Vinayachandran

*Centre for Atmospheric and Oceanic Sciences, Indian Institute of Science, Bangalore, India*

\*Corresponding author address: A. Sanchez-Franks, National Oceanography Centre, European  
Way, Southampton, UK, SO14 3ZH  
E-mail: alsf@noc.ac.uk

## ABSTRACT

15 In the Bay of Bengal (BoB), surface heat fluxes play a key role in monsoon  
16 dynamics and prediction. The accurate representation of large-scale surface  
17 fluxes is dependent on the quality of gridded reanalysis products. Meteorological  
18 and surface flux variables from five reanalysis products are compared  
19 and evaluated against in situ data from the RAMA moored array in the BoB.  
20 The reanalysis products: ERA-Interim (ERA-I), TropFlux, MERRA-2, JRA-  
21 55 and CFSR are assessed for their characterisation of air-sea fluxes during  
22 the southwest monsoon season (JJAS). ERA-I captured radiative fluxes best  
23 while TropFlux captured turbulent and net heat fluxes ( $Q_{net}$ ) best, and both  
24 products outperformed JRA-55, MERRA-2 and CFSR, showing highest correlations  
25 and smallest biases when compared to the in situ data. In all five  
26 products, the largest errors were in shortwave radiation ( $Q_{SW}$ ) and latent heat  
27 flux ( $Q_{LH}$ ), with non-negligible biases up to  $\sim 75 \text{ W m}^{-2}$ . The  $Q_{SW}$  and  $Q_{LH}$   
28 are the largest drivers of the observed  $Q_{net}$  variability, thus highlighting the  
29 importance of the results from the buoy comparison. There are also spatially  
30 coherent differences in the mean basin-wide fields of surface flux variables  
31 from the reanalysis products, indicating that the biases at the buoy position are  
32 not localized. Biases of this magnitude have severe implications on reanalysis  
33 products ability to capture the variability of monsoon processes. Hence, the  
34 representation of intraseasonal variability was investigated through the boreal  
35 summer intraseasonal oscillation and we found that TropFlux and ERA-I perform  
36 best at capturing intraseasonal climate variability during the southwest  
37 monsoon season.

## 38 1. Introduction

39 Circulation in the Indian Ocean is governed by monsoon variability (Lau et al. 2012; Weller  
40 et al. 2016). In the Bay of Bengal (BoB), sea surface temperature (SST) and heat flux are the  
41 key components in southwest (SW) monsoon behavior (Vecchi and Harrison 2002; Parampil et al.  
42 2010; Vialard et al. 2011). The mechanism via which the surface net heat fluxes ( $Q_{net}$ ) impact  
43 SST variability is linked to the BoB barrier layer (Duncan and Han 2009). During the summer,  
44 a combination of increased precipitation and river runoff in the northern BoB contributes to the  
45 formation of a highly stratified surface barrier layer that sits above the thermocline and below the  
46 mixed layer base (Vinayachandran et al. 2002). The summer barrier layer acts to inhibit processes  
47 such as entrainment, vertical advection and upwelling, which result in surface  $Q_{net}$  having a greater  
48 impact on the intraseasonal SST variability (Duncan and Han 2009).

49 The importance of the  $Q_{net}$  as a driver of summer SST variability in the BoB (Duncan and Han  
50 2009; Lau et al. 2012) is also shown in observations and ocean models, where summer intrasea-  
51 sonal oscillations (ISO) of SST are forced mainly by heat flux variability, with occasional contri-  
52 butions from vertical mixing and entrainment at the base of the mixed layer (Schiller and Godfrey  
53 2003; Waliser 2006; Girishkumar et al. 2017). Both models and observations indicate that the  
54 intraseasonal oscillation of the northern Indian Ocean SST impacts the large-scale atmospheric  
55 wind field, temperature, humidity and the active–break cycle of monsoon convection (Vecchi and  
56 Harrison 2002; Waliser 2006; Yang et al. 2008). Studies suggest that fluctuations in SST, driven  
57 by surface heat fluxes ( $Q_{net}$ ), can be used as an indicator/proxy for the forecast of active and break  
58 periods in the monsoon (Vecchi and Harrison 2002; Parampil et al. 2010). Consequently, the accu-  
59 rate measurement and representation of SST and  $Q_{net}$  are critical in understanding and predicting

60 SW monsoon processes over the BoB (Vialard et al. 2011), and monsoon variability and dynamics  
61 (Vecchi and Harrison 2002).

62 Several studies have reported significant differences between flux products and in situ data in  
63 the Indian Ocean (e.g., Yu et al. 2007; McPhaden et al. 2009; Kumar et al. 2012; Goswami et al.  
64 2014; Weller et al. 2016). McPhaden et al. (2009) found that then-current numerical weather pre-  
65 diction (NWP) products underestimated  $Q_{net}$  by 40-60  $\text{W m}^{-2}$  compared with in situ estimates  
66 from a moored buoy near  $0^\circ$ ,  $80.5^\circ\text{E}$ . Their results suggested that the accumulation of these defi-  
67 ciencies in heat flux over time could result in  $2^\circ\text{C}$  errors in  $SST$ . Kumar et al. (2012) compared  
68 reanalysis products with moored buoy data in the global tropical oceans to create a blended flux  
69 product, TropFlux, which is based on fields from the best performing product: the European Centre  
70 for Medium-Range Weather Forecasts (ECMWF) ERA-Interim (ERA-I) (Dee et al. 2011). They  
71 found that older reanalyses had larger biases and rms differences than ERA-I when compared to  
72 the in situ data. Yu et al. (2007) compared NWP, reanalysis and blended products for annual, sea-  
73 sonal and interannual time scales in the Indian Ocean and found differences between 53 and 108  
74  $\text{W m}^{-2}$  for daily averaged measurements. Goswami et al. (2014) showed that the coupled Climate  
75 Forecast System Reanalysis (CFSR) product does not accurately simulate monsoon intraseasonal  
76 variability. These studies highlight significant shortcomings with reanalysis fields in the Indian  
77 Ocean and suggest that the accumulated errors found in reanalysis and blended products could  
78 lead to significant deficiencies in their representation of Indian Ocean processes.

79 To determine whether any reanalysis product gives a robust representation of monsoon pro-  
80 cesses, particularly in the BoB, it is important to understand their individual performance in rep-  
81 resenting air-sea fluxes and related meteorological parameters, such as  $SST$ , surface wind speed  
82 ( $V$ ), air temperature ( $T_a$ ), and specific humidity ( $q_a$ ). The products examined in this work include  
83 the atmospheric global reanalysis products: ERA-I (Dee et al. 2011), the National Aeronautics

84 and Space Administrations (NASA) Modern Era Retrospective-Analysis for Research and Ap-  
85 plications v2 (MERRA-2) (Rienecker et al. 2011), the Japanese Meteorological Agency (JMA)  
86 Japanese 55-year Reanalysis (JRA-55) (Kobayashi et al. 2015), the National Centers for Envi-  
87 ronmental Prediction (NCEP) CFSR (Saha et al. 2010), and the air-sea flux product focused on  
88 the tropical oceans, TropFlux (Kumar et al. 2012). The products are assessed using in situ data  
89 from the Research Moored Array for African-Asian-Australian Monsoon Analysis and Prediction  
90 (RAMA) (McPhaden et al. 2009). The BoB is a region where monsoon processes are still not fully  
91 understood (Weller et al. 2016) and in situ data are sparse (Vinayachandran et al. 2018), making  
92 gridded reanalysis products hard to verify.

93 Section 2 gives a brief overview of the datasets used in this paper, including four reanalysis  
94 products, a blended product, and in situ data. The analysis and discussion of air-sea fluxes in the  
95 BoB for the SW monsoon season (JJAS) is presented in sections 3, 4 and 5. There is a comparison  
96 of reanalysis products with in situ data from RAMA buoys in the BoB for interannual variability  
97 (section 3), an in-depth analysis of individual flux components (section 4), and an evaluation of the  
98 reanalysis products characterisation of basin-wide air-sea fluxes and the associated intraseasonal  
99 variability from the boreal summer intraseasonal oscillation (section 5). A summary is given in  
100 section 6.

## 101 2. Data and Methods

102 The characterisation of air-sea fluxes in the BoB from flux products is investigated using mete-  
103 orological ( $SST$ ,  $V$ ,  $T_a$ ,  $q_a$ ) and flux parameters [shortwave radiation ( $Q_{SW}$ ), longwave radiation  
104 ( $Q_{LW}$ ), sensible heat flux ( $Q_{SH}$ ), latent heat flux ( $Q_{LH}$ ) and  $Q_{net}$ ] from four reanalysis products,  
105 one blended product, and in situ data from the RAMA moored array. The surface fluxes from the  
106 reanalysis products are model fluxes, turbulent fluxes for RAMA and TropFlux are calculated from

meteorological parameters following Fairall et al. (2003), radiative fluxes are measured by RAMA and derived as described in Kumar et al. (2012) for TropFlux. In all reanalysis (and blended) datasets,  $T_a$  and  $q_a$  are provided at 2 m height above sea level, and  $V$  is provided at 10 m. The in situ buoy data measures  $T_a$  and  $q_a$  at 3 m, and  $V$  at 4 m, which are adjusted to 2 m and 10 m respectively using COARE v3.0 algorithm (Fairall et al. 2003). Note,  $q_a$  is not available from ERA-I or at the RAMA sites. Instead, we use dewpoint temperature from ERA-I and relative humidity in the case of RAMA, from which we derive the vapour pressure ( $e$ ) and thus calculate  $q_a$ , as per Bolton (1980):

$$q_a = \left[ \epsilon \frac{e}{p - e(1 - \epsilon)} \right] \times 1000 \quad (1)$$

where  $p$  is surface pressure and  $\epsilon = 0.622$  is the ratio of the molecular masses of water vapour and dry air. Similarly the specific humidity at the sea surface,  $q_s$ , is computed from  $SST$  as per equation (1), where the saturation specific humidity is assumed to be at 98% saturation at the  $SST$ .

Data were obtained at the temporal resolutions described in section 2a for the summer periods (JJAS) from 2007 to 2015 and then daily averaged, as daily resolution is adequate for resolving intraseasonal variability which is the primary mode of variability for monsoonal processes. In the following sections, both meteorological and flux variables from the reanalysis data have been regridded to  $1^\circ \times 1^\circ$ , by linear interpolation, where necessary. The data products used in this paper are briefly described here and in Table 1.

#### *a. Reanalysis and blended products*

ERA-I is a global atmospheric reanalysis product from the ECMWF (Dee et al. 2011). The ERA-I data assimilation system uses 4-dimensional variational analysis (4D Var), with an improved hydrological cycle and quality control compared with the previous ECMWF reanalysis product: ERA-40 (Berrisford et al. 2011). The mean state variables used here are from the analysis field



129 (step 0) at 6-hourly time intervals and the flux variables are from the forecast field (step 12) at  
130 3-hourly time intervals. All variables are obtained on a  $1^\circ \times 1^\circ$  horizontal grid.

131 TropFlux is a blended (reanalysis-based) product of air-sea fluxes and associated meteorological  
132 variables over the global tropical oceans, from  $30^\circ\text{S}$  to  $30^\circ\text{N}$  (Kumar et al. 2012, hereafter KP12).  
133 TropFlux uses ISCCP satellite cloud data (Zhang et al. 2004) to compute  $Q_{SW}$ , and bias-adjusted  
134 ERA-I (Dee and Uppala 2009) data to compute  $SST$ ,  $V$ ,  $T_a$ ,  $q_a$  and  $Q_{LW}$  as per:

$$\Psi_{tf}(x,y,t) = a(\Psi(x,y,t) - \bar{\Psi}(x,y)) + b(x,y) + \bar{\Psi}(x,y) \quad (2)$$

135 where  $\Psi_{tf}$  is the corrected ERA-I variable,  $\Psi$ , and the long term mean is  $\bar{\Psi}$ . The amplitude,  $a$ , and  
136 bias,  $b$ , adjustments of the TropFlux variables are based on a comparison between the reanalysis  
137 product and in situ data from the Global Tropical Moored Buoy Array (McPhaden 2010). The  
138 turbulent fluxes were computed using the COARE v3.0 algorithm (Fairall et al. 2003) on the  
139 corrected daily-averaged input variables and, since TropFlux computes heat fluxes from daily  
140 averaged data, a gustiness correction is applied to the surface wind speed parameter to compensate  
141 for the higher frequency ( $< 1$  day) fluctuations in wind speed, which result in underestimations  
142 in the flux variability based on results of Cronin et al. (2006). The cool skin and warm layer  
143 calculations in COARE v3.0 are switched off (Kumar et al. 2012). The gustiness correction is  
144 applied to the surface wind speed parameter only for the computation of turbulent heat fluxes. The  
145 TropFlux data are served as daily means, on a  $1^\circ \times 1^\circ$  horizontal grid. The spatially homogeneous  
146 amplitude adjustment ( $a$ ) acts to increase the variance of all the parameters in ERA-I around  
147 their long term values. We note that TropFlux adjusts ERA-I meteorological parameters based  
148 on measurements from the Global Tropical Moored Buoy Array, however, only data to the end  
149 of 2009 was available at the time TropFlux was produced. At this time the RAMA array had  
150 only recently been established: measurements at b28 started in November 2006, with b26 and

151 b27 being added a year later. The observational constraints will therefore be dominated by the  
152 longer-established moorings in the Pacific, and to a lesser extent, in the Atlantic.

153 JRA-55 is the second global atmospheric reanalysis product produced by the JMA (Kobayashi  
154 et al. 2015), built to improve upon JRA-25 (Onogi et al. 2007). JRA-55 has a new longwave  
155 radiation scheme, increased spatial resolution, and uses variational bias correction (VarBC) and  
156 4D Var analysis. The data used here are on a  $0.56^\circ \times 0.56^\circ$  grid using analysis fields for the mean  
157 state variables and 3-hourly averages for the flux variables.

158 MERRA-2 is a global atmospheric reanalysis of the satellite period produced by NASA  
159 (Bosilovich et al. 2015), and updated from the original MERRA product (Rienecker et al. 2011).  
160 MERRA-2 uses an updated atmospheric data assimilation system: the Goddard Earth Observing  
161 System (GEOS-5) with a 3D Var algorithm. Important updates to MERRA-2 since the origi-  
162 nal MERRA product also include an updated observing system with more satellite observations,  
163 and an aerosol analysis (Bosilovich et al. 2015). The MERRA-2 data has a spatial resolution of  
164  $0.5^\circ$  latitude by  $0.625^\circ$  longitude on 72 levels. Here, the mean state variables are at 1-hourly, in-  
165 stantaneous, single-level diagnostics and the flux variables are 1-hourly, time-averaged, radiation  
166 diagnostics.

167 CFSR is a coupled ocean-atmosphere reanalysis product created by the NCEP (Saha et al. 2010).  
168 The Coupled Forecast System model that CFSR uses includes a spectral atmospheric model and  
169 the Modular Ocean Model from the Geophysical Fluid Dynamics Laboratory. The atmospheric  
170 model has a spatial resolution of  $0.5^\circ \times 0.5^\circ$  on 37 vertical levels, and the ocean model has a  
171 resolution of  $0.5^\circ$  on 40 vertical levels. CFSR was completed for the period of 1979 to 2009  
172 and was later extended to 2011. In 2011, CFSv2 was implemented as a continuation of CFSR  
173 (Saha et al. 2011). As CFSv2 uses the same model as CFSR, the CFSv2 product is treated as  
174 an extension of CFSR and CFSv2 is hereafter implied in any mention of CFSR. The data were

175 available at 6-hour forecast field for mean state variables and at 6-hour averaged field for flux  
176 variables.

177 All reanalysis products assimilate ocean observations from fixed mooring arrays, including the  
178 Global Tropical Moored Array (McPhaden 2010).

179 *b. In situ data: the RAMA array*

180 RAMA is an array of moored buoys in the Indian Ocean that provide atmospheric and oceano-  
181 graphic data for the study of ocean circulation, air-sea interactions and monsoon dynamics  
182 (McPhaden et al. 2009). The types of moored buoys relevant for this study within the RAMA  
183 network are the surface and enhanced surface moorings. The enhanced surface moorings are Au-  
184 tonomous Temperature Line Acquisition System (ATLAS) moorings with additional sensors for  
185 pressure and longwave radiation measurements designed for measuring complete air-sea interac-  
186 tions, and are denominated flux reference sites. In the BoB, there are two surface moorings located  
187 at 8°N, 90°E (designated b26) and 12°N, 90°E (b27), and one enhanced surface mooring at 15°N,  
188 90°E (b28).

189 Meteorological variables used include *SST* (measured at 1 m below sea surface), *V* (measured  
190 at 4 m above sea surface and converted to 10 m height by the data providers), *T<sub>a</sub>* (measured  
191 at 3 m above sea surface and adjusted to 2 m), and relative humidity (measured at 3 m above  
192 sea surface and adjusted to 2 m), *T<sub>a</sub>* and pressure from which *q<sub>a</sub>* is computed as per equation  
193 (1). All height adjustments use the COARE v3.0 algorithm as per Fairall et al. (2003). Table  
194 2 shows the uncertainties for the meteorological variables (*SST*, *V*, *T<sub>a</sub>*, humidity), which corre-  
195 spond to the Next Generation ATLAS Mooring Sensors accuracies listed on the NOAA/PMEL  
196 website, <https://www.pmel.noaa.gov/gtmba/sensor-specifications>. These accuracies are based on

197 calibrations for pre-deployment and post-recovery.  $\Delta T$  and  $\Delta q$  uncertainties are calculated using  
 198 quadrature (Table 2).

199 The air-sea flux variables are computed using the COARE 3.0b algorithm (Fairall et al. 2003;  
 200 Cronin et al. 2006) by data providers. Net radiative fluxes, also calculated by providers, were  
 201 calculated from measured downwelling components following Cronin et al. (2006) such that:

$$Q_{SW} = (1 - \alpha) \times SWR \quad (3)$$

202

$$Q_{LW} = \varepsilon(\beta \times T_s^4 - LWR) \quad (4)$$

203 where  $\alpha$  is a constant albedo value of 0.055, SWR is the incoming downwelling radiation,  $\varepsilon$   
 204 is the emissivity constant (0.97),  $\beta$  is the Stefan Boltzman constant ( $5.67 \times 10^{-8}$ ),  $T_s$  is the skin  
 205 temperature (K) and LWR is the incoming downwelling longwave radiation. For the turbulent  
 206 fluxes, biases from daily resolved wind speed in the RAMA fluxes (computed using COARE 3.0)  
 207 are minimized by applying a gustiness correction in the wind speeds prior to their use in the bulk  
 208 flux calculations as per Cronin et al. (2006). We estimated the turbulent flux uncertainties (Table  
 209 2) from the standard deviation of differences between RAMA turbulent fluxes (calculated using  
 210 hourly data input for the COARE3.0 algorithm, including cool skin and warm layer effects) and  
 211 turbulent fluxes estimated from RAMA meteorological variables perturbed with the instrument  
 212 uncertainties (input data was daily averaged in the COARE3.0 algorithm, and as per Cronin et al.  
 213 (2006) cool skin and warm layer effects were turned off). We note that there is a mean difference  
 214 of 0.13 and  $2.25 \text{ W m}^{-2}$  for  $Q_{SH}$  and  $Q_{LH}$  respectively when comparing turbulent fluxes estimated  
 215 from hourly averaged data (cool skin and warm layer effects turned on) and daily averaged data  
 216 (cool skin and warm layer turned off). Subsets of RAMA data can be obtained from the TAO  
 217 Project Office of NOAA/PMEL, where meteorological and flux variables are available at high (up

218 to 10 min) resolution. All meteorological and flux variables are presented in this paper averaged  
219 to give daily resolution.

220 The RAMA moorings in the BoB have been operational since 2007; however, issues in buoy  
221 maintenance affect data return resulting in intermittent data coverage (McPhaden 2010). Fig. 1  
222 shows the availability of parameters used in this study at b28. As b27 and b26 are not flux reference  
223 sites, pressure (hence  $q_a$ ) and  $Q_{LW}$  are not available at these buoy locations (not shown here).  
224 The most comprehensive coverage occurs at site b28, with almost complete data return in  $SST$ .  
225 Noticeable gaps for the remaining variables occur mostly during 2007, 2008, 2011, 2012 and (for  
226  $V$  and turbulent fluxes only) 2013. Due to the data limitation at sites b27 and b26, the following  
227 time series analysis using reanalysis products and the RAMA buoys will focus only on data from  
228 site b28.

### 229 **3. Evaluation of meteorological and flux variables**

230 In this section, the five data products are evaluated against in situ data from the RAMA buoy b28  
231 in the BoB for the summer months (JJAS), from 2007 to 2015. We evaluate the meteorological  
232 parameters important for calculation of turbulent fluxes:  $SST$ ,  $V$ ,  $T_a$  and  $q_a$ , as well as the air-  
233 sea temperature difference,  $\Delta T$ , the air-sea humidity difference,  $\Delta q$ , the turbulent fluxes,  $Q_{SH}$  and  
234  $Q_{LH}$ , the radiative fluxes,  $Q_{SW}$  and  $Q_{LW}$ , and the  $Q_{net}$ . In the following section, meteorological  
235 variables are further investigated to understand their impact on the turbulent fluxes in this region  
236 and the causes for disparities in the products' ability to represent surface fluxes.

237 Individual daily values of the surface fluxes and associated variables for each of the products are  
238 compared to RAMA b28 using four metrics. Firstly the differences (product - b28) and their 95%  
239 confidence intervals (calculated using a t test implemented in R using function `t.test` (R Core Team  
240 2015)) are presented (Fig. 2a). Second, the Pearson product moment correlation coefficients for

each product with b28 and their 95% confidence intervals (calculated in R using function cor.test) are presented (Fig. 2b). Fig. 2c shows the variance ratio of the parameters with their 95% confidence interval (calculated using an F test implemented in R using function var.test). Fig. 2d combines these metrics to give skill scores for each product and variable (Wallcraft et al. 2009). Skill scores are an established way to assess the quality of numerical weather forecasts (Murphy 1988) and are based on the correlation between the product being assessed and a reference standard, penalized for disagreement in mean values and variance ratio. Thus, if we denote  $x_i$  ( $i = 1, \dots, n$ ) as the observations and  $y_i$  ( $i = 1, \dots, n$ ) as a data product for a sample of  $n$ , we can define the linear correlation,  $R$ , and skill score,  $SS$ , between  $x_i$  and  $y_i$  as per Murphy (1988):

$$R = \frac{1}{n} \sum_{i=1}^n \frac{(x_i - \bar{\mathbf{x}})(y_i - \bar{\mathbf{y}})}{(\sigma_x \sigma_y)} \quad (5)$$

$$SS = R^2 - \left[ R - \frac{\sigma_y}{\sigma_x} \right]^2 - \left[ \frac{(\bar{\mathbf{y}} - \bar{\mathbf{x}})}{\sigma_x} \right]^2 \quad (6)$$

where  $\bar{\mathbf{x}}$ ,  $\bar{\mathbf{y}}$  and  $\sigma_x$ ,  $\sigma_y$  are the sample mean and standard deviation of  $x_i$  and  $y_i$ , respectively. Skill scores of 1 demonstrate perfect agreement between the data products and the observed data. Perfectly correlated data with a 25% underestimate of variance and a bias of magnitude of 25% of the variance would have a skill score of 0.5. Negative skill scores typically arose in our comparison due to substantial underestimates of variance combined with large mean differences, although there were also some low correlation values.

*Sea surface temperature* For *SST*, all reanalysis products show fairly strong correlations with RAMA b28 (Fig. 2b). ERA-I shows the largest offset (-0.37 °C), followed by MERRA-2 (-0.20 °C), both underestimating the in situ *SST* (Fig. 2a). Both these reanalyses use the OSTIA foundation *SST* product (Donlon et al. 2012) in the period of our analysis so are expected to have colder *SST*s than a standard near-surface estimate. MERRA-2 uses OSTIA after 2006 and ERA-I from February 2009, The reason for the difference between the *SST* for these products is

therefore not clear; their agreement improves from 2009 but remains  $0.2^{\circ}\text{C}$  (not shown). JRA-55 *SST* agrees well with b28, with the smallest bias and highest correlation (Fig. 2b, 0.90), giving the highest skill in reproducing the b28 *SST* (Fig. 2d), despite an underestimate of the variance (Fig. 2c). The coupled product CFSR also shows a good representation of the observed *SST*. We note that the CFSR *SST* is constrained through a relaxation coefficient at the sea surface (i.e. model *SST* is nudged toward observed *SST*), which counteracts any drift in the model related to error in the surface fluxes (Xue et al. 2011). On the other hand, JRA-55, MERRA-2, and ERA-I are atmosphere-only reanalysis products with prescribed *SST* fields (Table 1).

*Surface wind speed*  $V$  shows the highest correlation ( $\geq 0.9$ ) across all products with  $V$  from RAMA b28. TropFlux and MERRA-2  $V$  are closest to that from b28. ERA-I and JRA-55 underestimate and CFSR overestimates the observed  $V$  (Fig. 2a). Variance ratios are around one, apart from CFSR, which shows significantly greater variance in  $V$  than b28 (Fig. 2c).  $V$  shows the best skill scores across the variables with ERA-I, TropFlux and JRA all having skill scores of about 0.9 (Fig. 2d).

*Air Temperature* The highest  $T_a$  correlations are observed with ERA-I, TropFlux and JRA-55 ( $\geq 0.83$ ) and the lowest correlation with MERRA-2 (0.62) (Fig. 2b). ERA-I has the largest offset ( $-0.38^{\circ}\text{C}$ ), the other products are within  $0.1^{\circ}\text{C}$  of b28 (Fig. 2a). TropFlux significantly overestimates the variance, and MERRA-2 and CFSR significantly underestimate the variance (Fig. 2c). Overall JRA-55 shows the best skill, followed by TropFlux (Fig. 2d).

*Specific humidity* The products all struggle with reproducing the observed  $q_a$ . Kumar et al. (2012) found that ERA-I underestimated  $q_a$ , and attributed more than half of that estimate to a cold bias in  $T_a$  and the remainder to an underestimate in the relative humidity. However their adjustment to  $q_a$  for ERA-I for TropFlux results in an overestimate at b28. Skill scores are all

less than 0.2, resulting from a combination of modest correlations ( $< 0.8$ ), large mean biases ( $> 0.3 \text{ g kg}^{-1}$ ), and a large underestimate of the variance. Our results show a CFSR dry bias also previously observed in the maritime continent and western Pacific by Wang et al. (2011) and overall dry bias found in ERA-I when compared to research vessel data (Brunke et al. 2011).

*Air-sea temperature difference* For all products except ERA-I, the skill scores for  $\Delta T$  are much lower than those for either  $SST$  or  $T_a$  (Fig. 2d). JRA-55 performs best, combining a small bias (Fig. 2a) with the strongest correlation (Fig. 2b) and is the only product to make a reasonable estimate of the variance (Fig. 2c).

*Air-sea humidity difference* The skill scores for  $\Delta q$  for ERA-I, JRA-55 and MERRA-2 are larger than their respective skill scores for  $q_a$ , but the best skill score is only 0.5 for MERRA-2 (Fig. 2d). Modest correlations combined with large biases for most products (Fig. 2a) and a very significant underestimate of variance (Fig. 2c) give poor skill overall.

*Shortwave radiation* For all products apart from TropFlux, biases in  $Q_{SW}$  (and  $Q_{LW}$ ) are directly linked to its radiation schemes, spatial distribution and aerosol properties (Dee et al. 2011). TropFlux  $Q_{SW}$  uses observed cloudiness data from ISCCP up until the end of 2007 (when it was last available), and the ISCCP mean seasonal cycle and adjusted using NOAA outgoing longwave radiation (OLR) thereafter (KP12). TropFlux and ERA-I show the highest correlations ( $\sim 0.7$ ) with the observed  $Q_{SW}$  (Fig. 2b) and the highest overall skill (Fig. 2d). All of the products underestimate  $Q_{SW}$  apart from CFSR which overestimates by more than  $70 \text{ W m}^{-2}$ . MERRA-2 and CFSR show the lowest correlations (Fig. 2b) and highest biases (Fig. 2a). Positive bias in CFSR  $Q_{SW}$  in the tropics has been previously catalogued by Wang et al. (2011) due to an underestimate of cloudiness. MERRA-2s underestimation of  $Q_{SW}$  has been similarly linked to its cloud scheme



308 (general difficulties capturing irradiance variability) in a study by Boilley and Wald (2015). All of  
309 the products significantly underestimate the variability of  $Q_{SW}$  (Fig. 2c).

310 *Longwave radiation* The skill scores for  $Q_{LW}$  are very low, with only ERA-I achieving a positive  
311 score (Fig. 2d). All products underestimate the variance (Fig. 2c) and for all of the products other  
312 than ERA-I the biases are large relative to the variability resulting in low skill.

313 *Sensible heat flux* TropFlux has the most skill due to a relatively high correlation of 0.79, a small  
314 bias of slightly over  $1 \text{ W m}^{-2}$  but overestimates the variance. ERA-I and JRA-55 have negative  
315 skill scores due to large biases and overestimates of variance. The poor skill in JRA-55 is hard to  
316 understand as it performed best at reproducing  $\Delta T$  and showed high skill for  $V$ .

317 *Latent heat flux* TropFlux is the only product to have a positive skill score for  $Q_{LH}$ . This is sur-  
318 prising as it had relatively poor skill for  $\Delta q$  (Fig. 2d). TropFlux underestimates  $\Delta q$  but shows only  
319 a small underestimate in  $Q_{LH}$  which may indicate that the gustiness parameter used by TropFlux  
320 in the transfer coefficients may be acting to compensate for low  $\Delta q$  with an enhanced wind effect  
321 in the flux calculation. MERRA-2s large overestimation of  $Q_{LH}$  can be attributed to the fact that  
322 MERRA-2 has humidity (dry) bias problems related to forecast model spin up/down (Kobayashi  
323 et al. 2015). The large  $Q_{LH}$  bias apparent in CFSR has been observed on a global scale (larger  
324 evaporative cooling, in general) and is linked to the dry bias over the equatorial Indian Ocean  
325 (Wang et al. 2011) and the erroneously strong winds (Fig. 2a).

326 *Net heat flux* TropFlux has the highest skill in reproducing  $Q_{net}$ . CFSR does better than expected,  
327 despite having negative skill scores for 3 of the 4 flux components, and ERA-I is the only other  
328 product to have a positive skill score (Fig. 2d). ERA-I, JRA-55 and MERRA-2 all have too much  
329 heat loss from the ocean. TropFlux and CFSR all show a mean net heat gain by the ocean of  
330  $30\text{-}35 \text{ W m}^{-2}$  over JJAS of 2007-2015, whereas ERA-I, JRA-55 and MERRA-2 all show a net

331 heat loss of between  $-20$  to  $-50 \text{ W m}^{-2}$  (not shown here). We note that biases in turbulent and  
 332 radiative fluxes cancel out in the  $Q_{net}$  from CFSR and (to a smaller degree) TropFlux. However,  
 333 biases (mostly) in  $Q_{SW}$  and  $Q_{LH}$  carry over considerably in the  $Q_{net}$  biases estimated from ERA-I,  
 334 JRA-55 and MERRA-2. Thus the blended product, TropFlux, captures the observed  $Q_{net}$  with  
 335 greater skill than the reanalysis products.

336 Similar results are found between the reanalysis products and in situ data at other BoB RAMA  
 337 buoy locations:  $90^\circ\text{E}$ ,  $12^\circ\text{N}$  (b27; Fig. S1) and  $90^\circ\text{E}$ ,  $8^\circ\text{N}$  (b26; Fig. S2). Based on the 4 metrics  
 338 presented here,  $SST$  and  $V$  perform consistently well at all 3 locations;  $T_a$  struggles showing lower  
 339 correlations and poorer skill scores at b27 and b26 (more so than at b28) and as a result  $\Delta T$  and  
 340  $Q_{SH}$  are similarly poorly represented across most products. For  $Q_{LH}$ , results are consistently poor  
 341 and only TropFlux shows a skill score greater than zero. Last,  $Q_{SW}$  performs similarly between  
 342 products for all 3 buoys, i.e. ERA-I and TropFlux are able to reasonably reproduce  $Q_{SW}$  while  
 343 remaining products perform poorly based on mean differences, correlations, variance ratio and  
 344 skill score.

345 Based on the four metrics presented here, we find that ERA-I captures radiative fluxes best while  
 346 TropFlux is better at capturing the turbulent and net heat fluxes. In general, however,  $Q_{SW}$  and  $Q_{LH}$   
 347 (and  $Q_{net}$  by association) are the variables that are the hardest to capture across all products. This  
 348 is evident in the low correlations, large biases and low skill scores. Since errors in  $Q_{net}$  can cause  
 349 large errors in  $SST$  in the BoB and affect the accurate representation of monsoon processes from  
 350 reanalysis products, the next section investigates the flux components in more depth.

#### 351 **4. Surface Fluxes at RAMA flux reference site b28**

352  $SST$  variability in the BoB is mainly driven by surface heat fluxes (Sengupta and Ravichandan  
 353 2001). Accurate representation of meteorological variables and the associated fluxes in reanalysis

products is therefore crucial for the correct representation of monsoon related variability. The individual components of surface heat fluxes are further investigated here.

Fig. 3 shows scatterplots of the  $Q_{net}$  vs each flux component from RAMA b28, ERA-I, TropFlux, JRA-55, MERRA-2 and CFSR. Individual daily means are plotted as points and contour lines enclose 10% and 50% of points in the each joint distribution (calculated with R function HPDregionplot in the emdbook package, Bolker (2008)). Fig. 3a shows the relationship between  $Q_{SW}$  and  $Q_{net}$  at b28.  $Q_{SW}$  is the main driver of  $Q_{net}$  with a strong positive correlation ( $r=0.93$ ).  $Q_{LW}$  is anticorrelated with  $Q_{net}$  ( $r=-0.58$ , Fig. 3b) as increased cloud cover reduces the heat gain by the ocean by  $Q_{SW}$  and reduces the heat loss by the ocean by  $Q_{LW}$ . Both  $Q_{LH}$  and  $Q_{SH}$  are positively correlated with  $Q_{net}$  ( $r=0.68, 0.63$  respectively, Fig. 3c,d) but  $Q_{LH}$  is an order of magnitude larger.

ERA-I shows similar correlations to b28, the correlations for the radiative components ( $Q_{SW}$  and  $Q_{LW}$ ) being slightly less correlated with  $Q_{net}$  than for B28 and the turbulent components ( $Q_{LH}$  and  $Q_{SH}$ ) more correlated. The underestimate of variability in  $Q_{SW}$  and  $Q_{LW}$  by ERA-I is clear in Figs. 3e, f, and the overestimate of  $Q_{LH}$  and resulting bias in  $Q_{net}$  in Fig. 3g. The adjustments applied to ERA-I to give TropFlux perform well for the turbulent fluxes (Figs. 3k, l) given better alignment of the distributions in addition to reducing biases. However the radiative estimates from TropFlux are worse than ERA-I. TropFlux  $Q_{SW}$  is constructed from ISCCP, until 2007, and bias corrected ISCCP mean seasonal cycle and NOAA OLR to present; hence, TropFlux  $Q_{SW}$  biases are likely linked to the algorithm used in KP12. TropFlux  $Q_{SW}$  shows improved (higher) variability, but shifts the peak of the distribution to even lower values than ERA-I (compare Figs. 3e, i). The adjustments applied to ERA-I  $Q_{LW}$  to give TropFlux give worse performance compared with b28 (Figs. 3f, j).

The remaining 3 products (JRA-55, MERRA-2 and CRSR, Figs. 3m-x) all show poor agreement with the relationships between the flux components and  $Q_{net}$ , as expected from the skill scores

presented in Fig. 2. The exception is the good agreement shown for CFSR  $Q_{SH}$  (Fig. 3x) but only due to the compensating biases in CFSR  $Q_{net}$ .

De-constructing turbulent fluxes into their meteorological components provides further insight into differences among products, and helps determine if errors and biases in  $Q_{SH}$  ( $Q_{LH}$ ) at the buoy location (Fig. 2a) originate from errors in the wind field or air-sea contrasts in temperature (humidity). Fig. 4a-f shows scatterplots of  $Q_{LH}$  vs the individual components of  $Q_{LH}$ :  $\Delta q$  and  $V$ . The largest contributing factor to  $Q_{LH}$  variability across all products is  $V$ , where increases in  $V$  are linked with increases in  $Q_{LH}$  (Fig. 4d). The correlation between  $\Delta q$  and  $Q_{LH}$  is lower (Fig. 4a) as  $\Delta q$  and  $V$  are anti-correlated (Fig. 4g). This anti-correlation is well-captured by ERA-I (Fig. 4h) with a slight overestimate of  $\Delta q$ . The TropFlux corrections result in a underestimation of  $\Delta q$ , but despite this the  $Q_{LH}$  agrees reasonably with b28, perhaps due to the gustiness adjustment to wind in the flux calculation.

$\Delta T$  is the strongest control on  $Q_{SH}$  (Fig. 4j) with  $V$  contributing little to the variability (Fig. 4m) of  $Q_{SH}$ . This is consistent with the finding that  $Q_{SH}$  variability is particularly sensitive to  $SST$  fluctuations (compared to  $Q_{LH}$ ) in the tropical Indian Ocean at intraseasonal time scales (DeMott et al. 2014). Both ERA-I (Fig. 4k) and TropFlux (Fig. 4l) overestimate the variability in  $\Delta T$ . ERA-I is biased toward unstable atmospheric conditions ( $\Delta T$  positive) and TropFlux over-represents stable conditions. The TropFlux  $Q_{SH}$  is strongly skewed compared to b28, but the representation of  $Q_{SH}$  is overall better than ERA-I (Fig. 2d). The relationship between the radiative flux components at b28 (Fig. 4s) is better captured by ERA-I (Fig. 4t) than TropFlux (Fig. 4u).

In general,  $Q_{net}$  is largely driven by  $Q_{SW}$  and  $Q_{LH}$ ;  $Q_{LH}$  variability is driven by  $V$  and (to a lesser extent)  $\Delta q$ , and  $Q_{SH}$  variability is mostly driven by  $\Delta T$ . Results here suggest errors/biases in  $Q_{LH}$  originate from both the wind field and the  $\Delta q$  and, as  $Q_{SH}$  shows negligible dependence on  $V$ , the

biases from the observed  $Q_{SH}$  are more likely to be linked with errors in the  $\Delta T$ .  $Q_{SW}$  and  $Q_{LH}$  are the variables the reanalysis and blended products have the most difficulty reproducing (Section 3).

## 5. Air-Sea fluxes across the Bay of Bengal

### *a. Mean fields*

In this section, air-sea fluxes at all points in the BoB from the reanalysis products are compared to determine how much of the variability observed at the RAMA buoy sites is localized.

Figure 5 shows turbulent fluxes from five data products averaged over the summer (JJAS) monsoon season, from 2007 to 2015, across the BoB. The  $Q_{SH}$  values from JRA-55 and (to a lesser extent) ERA-I show higher negative (upward) flux values, indicating greater heat loss from ocean to atmosphere, than the other 3 products. This is consistent with biases seen in section 3 (Fig. 2a), where JRA-55 and ERA-I overestimated the observed  $Q_{SH}$ . Differences in spatial gradients between products occur near b28 (black square, Fig. 5), where TropFlux, ERA-I and CFSR show a larger gradient decreasing from east to west across the buoy, and MERRA-2 and JRA-55 show almost no gradient. Other spatial differences are apparent in the patterns across coastal waters of the BoB, such as the region around Sri Lanka and the east coast of India, where only TropFlux and CFSR show regions of positive  $Q_{SH}$  (i.e. heat gain to the ocean). (We note the smaller contour range in  $Q_{SH}$  values,  $-20$  to  $20 \text{ W m}^{-2}$  compared with  $Q_{LH}$ ,  $-200$  to  $0 \text{ W m}^{-2}$ ). For the mean  $Q_{LH}$  field, all products show a region of strong  $Q_{LH}$  centred on the southern part of the BoB, sandwiched between the equator and  $10^\circ\text{N}$ , covering the zonal extent of the basin. This pool of elevated  $Q_{LH}$  in the southern BoB appears largest and strongest in JRA-55 and CFSR, and in TropFlux the pool is shifted further south and is considerably weaker compared to the remaining reanalysis products. Near b28 most products show a strong gradient in  $Q_{LH}$  decreasing from south

to north, though in JRA-55 this gradient is slightly more sloped in the southwest to northeast direction. These patterns are consistent with the mean and standard deviation of the  $Q_{SH}$  and  $Q_{LH}$  from all products (Fig. S3). Combining these results with the biases and skill scores from section 3, where it was shown that  $Q_{LH}$  from TropFlux underestimates the observed  $Q_{LH}$  at b28 and the reanalysis products all overestimate the observed  $Q_{LH}$  by a wide margin on the order of 50 to 75  $\text{W m}^{-2}$ , suggests TropFlux captures turbulent fluxes best, and the erroneously enhanced  $Q_{LH}$  seen at the b28 location in ERA-I, JRA-55, MERRA-2 and CFSR shows large-scale coherence across the BoB.

In section 3,  $Q_{SW}$  was shown to have some of the largest biases in the reanalysis products when compared with the in situ  $Q_{SW}$  from RAMA b28 data. It follows that in Fig. 6, the mean  $Q_{SW}$  fields over the BoB show a wide range in  $Q_{SW}$  values ( $\sim 100$  to  $250 \text{ W m}^{-2}$ ), differing quite substantially between products: CFSR and MERRA-2 show higher and lower values, respectively, of  $Q_{SW}$  when compared to ERA-I, TropFlux and JRA-55. The mean  $Q_{SW}$  field across the BoB depicts regions of high  $Q_{SW}$  in the vicinity of Sri Lanka and southwest of the southernmost tip of India, from the equator to  $5^\circ\text{N}$  in ERA-I, in TropFlux and JRA-55, but not in the MERRA-2 or CFSR products, consistent with dry slot in the rain shadow of Sri Lanka (Puvaneswaran and Smithson 1991). Since the smallest biases (which are negative) were observed in JRA-55 and ERA-I in section 3 (Fig. 2a), these results suggest TropFlux and (to a greater degree) MERRA-2 values are underestimating the observed  $Q_{SW}$  across the basin, while CFSR is overestimating them across the basin on an order of  $70 \text{ W m}^{-2}$ . CFSR also shows the greatest departure from the spatial patterns across the BoB than any of the other products, failing to capture the region of high  $Q_{SW}$  around Sri Lanka and southeast India (Fig. S3). The difference in the range of  $Q_{LW}$  values across products is considerably smaller, consistent with section 3, where it was shown that the  $Q_{LW}$  had some of the smallest biases among the flux components (Fig. 2a). The mean field for  $Q_{LW}$  appears

447 to show a more consistent pattern in spatial gradients from all products across the BoB, compared  
448 to  $Q_{SW}$  (Fig. 6; right hand column). In general, there is a high to low (south to north) gradient in  
449  $Q_{LW}$  across the BoB.

450  $Q_{net}$  for ERA-I, JRA-55 and MERRA-2 depict large heat loss in the central and southern regions  
451 of the BoB (Fig. S4), which is consistent with the results shown in section 3 (Fig. 2). TropFlux  
452 and CFSR, on the other hand, depict a net heat gain by the ocean all across the basin and strongest  
453 in the southwest and northern parts of the basin. In particular, values for  $Q_{net}$  in CFSR are the  
454 product of errors in the  $Q_{LH}$  and  $Q_{SW}$  components cancelling out. Since the patterns of variability  
455 are generally similar across the basin for all products (Fig. 6), results from section 3 wherein  
456 TropFlux underestimates observed  $Q_{LW}$  and all remaining products overestimate the observed  $Q_{LW}$   
457 at RAMA b28 (Fig. 2a) are taken to be representative of the basin wide biases in the BoB.

#### 458 *b. Monsoon Variability: The Boreal Summer Intraseasonal Oscillation*

459 In the previous sections, the performance of the reanalysis products in simulating the day-to-day  
460 variability at a point location in the BoB (sections 3, 4) and the time-mean spatial patterns over  
461 the BoB (section 5a) was assessed. Another necessary capability of a reanalysis product is that  
462 it should be able to simulate the main spatial and temporal patterns of variability within a given  
463 region, as these modes are the likely sources of potential predictability in a forecast system that  
464 uses reanalysis products as a forcing input. The boreal summer intraseasonal oscillation (BSISO)  
465 is one of the primary modes of variability associated with the Asian summer monsoon (Webster  
466 et al. 1998; Lee et al. 2013). The BSISO is also known as the Monsoon Intraseasonal Oscillation  
467 (MISO; Suhas et al. 2013), and was first identified as northward-propagating 30-60-day bands of  
468 clouds and convection over India by, e.g., Sikka and Gadgil (1980). It is often recognised as the  
469 northern summer counterpart to the Madden-Julian Oscillation (MJO; Madden and Julian, 1994).

470 Here the BSISO index from Lee et al. (2013) is used to assess the representation of boreal summer  
471 intraseasonal variability from the reanalysis products.

472 Similar to the MJO (Wheeler and Hendon 2004), the BSISO indices are constructed from multi-  
473 variate empirical orthogonal function analysis of satellite OLR and the 850-hPa zonal wind fields  
474 from NCEP-DOE reanalysis in the region of the Asian summer monsoon (Lee et al. 2013). The  
475 first two principal components (PC) of the BSISO form the BSISO1, which corresponds to the  
476 northward propagating component of the summer monsoon and has a 30–60 day period (Wang  
477 et al. 2005). The third and fourth PC of the BSISO form the BSISO2, which is the north-  
478 ward/northwestward component of the monsoon, usually associated with the pre-monsoon and  
479 monsoon onset periods, and has a period of 10–20 days (Kikuchi and Wang 2010). Here we focus  
480 on the 30–60 day northward propagating BSISO, i.e. the BSISO1.

481 The BSISO1 mode is divided into eight phases, each phase covering one-eighth of the cycle  
482 (Lee et al. 2013). During phase 1, a zonally elongated band of enhanced atmospheric convection  
483 lies over the equatorial Indian Ocean, while a band of suppressed convection extends from India  
484 southeastward across the BoB, southeast Asia and into the equatorial western Pacific (Fig. 7).  
485 Over phases 2, 3 and 4, the band of enhanced convection moves northward and eastward, while  
486 the suppressed convection retreats to the northeast and contracts. A second band of suppressed  
487 convection then starts to develop over the equatorial Indian Ocean, such that the anomalies at  
488 phase 5 are approximately the opposite sign to those at phase 1 (a half cycle earlier). The new  
489 band of suppressed convection then propagates northeastward during phases 6, 7, and 8. Finally,  
490 enhanced convection re-establishes itself over the equatorial Indian Ocean again in phase 1, and  
491 the next cycle begins.

492 The BSISO1 composites here are constructed using an index of BSISO1 phases (1–8) based on  
493 satellite OLR and 850hPa zonal wind fields as described in Lee et al. (2013) and made available



494 through the APEC Climate Centre data portal: <http://www.apcc21.net/ser/casts.do?lang=en>. For  
 495 each variable  $V$ , wind direction,  $Q_{SW}$ ,  $Q_{LH}$  and  $Q_{net}$ , daily anomalies were computed from the  
 496 monthly mean for the monsoon season (JJAS) 2007 to 2015. Then, each day during the study  
 497 period was allocated to one of the eight BSISO1 phases, or was discarded if the overall BSISO1  
 498 amplitude was weak (i.e.,  $\sqrt{PC1^2 + PC2^2} < 1$ ). Data from each product were averaged over the  
 499 days in each phase to obtain the eight phase composites of the life cycle.

500 The BSISO1 representations in each reanalysis product are first validated against the *in situ*  
 501 data at the RAMA b28 location. Fig. 8 shows the median, interquartile range, 95% confidence  
 502 intervals and outliers for  $V$ , wind direction,  $Q_{SW}$ ,  $Q_{LH}$  and  $Q_{net}$  from the in situ data and the ERA-  
 503 I, TropFlux and CFSR products at each phase of the BSISO1 life cycle. During phase 1 (2) all  
 504 products overestimate (underestimate) the observed BSISO1  $V$  and, in general, all do a reasonable  
 505 job of capturing the observed  $V$  during BSISO1 phases 3 to 8 (Fig. 8a-d). The prevailing surface  
 506 winds remain approximately from the south west during JJAS, as measured by the buoy and in all  
 507 the products at the buoy location (Fig. 8e-h). The change in surface wind direction through the  
 508 cycle is less well represented in the products. During phases 1 through 3, the buoy shows winds  
 509 becoming more southerly, whereas all of the products show a change to more westerly winds  
 510 during these phases.

511 The RAMA  $Q_{SW}$  measurements show high median values in phases 1 to 3 (Fig. 8i), during the  
 512 convectively suppressed part of the BSISO1 cycle in the northern BoB (Fig. 7). As the enhanced  
 513 convection moves into the BoB, cloud cover increases and the  $Q_{SW}$  values decrease during phases  
 514 4, 5 and 7. Although the reanalysis products do reproduce this qualitative pattern, they all under-  
 515 estimate the amplitude of the  $Q_{SW}$  variability associated with the BSISO1 (Fig. 8j-l). In particular,  
 516 ERA-I and TropFlux tend to underestimate (overestimate) highs (lows) in the observed  $Q_{SW}$  within  
 517 a range of  $\pm 45 \text{ W m}^{-2}$ ; meanwhile though CFSR also generally underestimates the amplitude of

the variability, it grossly overestimates  $Q_{SW}$  values (associated with BSISO1) in comparison with the observed  $Q_{SW}$ , with up to values of  $75 \text{ W m}^{-2}$ . These results are consistent with section 3, where it was shown that ERA-I and (to a lesser degree) TropFlux reasonably estimated the observed  $Q_{SW}$ , based on skill score; and, CFSR showed large positive biases, low correlation and poor skill score for  $Q_{SW}$ . Hence, in an ocean model forced by one of these products, the heating of the ocean surface by  $Q_{SW}$  during the suppressed convective phase, and the cooling during the active convective phase of the BSISO1 would both be severely misrepresented.

The systematic error apparent in  $Q_{SW}$  is compensated to a certain degree by a systematic error in  $Q_{LH}$  of similar magnitude (Fig. 8n-p). The  $Q_{LH}$  at the RAMA b28 location shows low median  $Q_{LH}$  values in phases 1 to 3, indicating reduced cooling of the ocean surface, and higher  $Q_{LH}$  values from phases 5 to 7, indicating increased cooling of the ocean surface (Fig. 8m). The TropFlux product does best at capturing the  $Q_{LH}$  BSISO1 variability and magnitude. The other data products appear to generally capture the observed variability correctly; however, both ERA-I and (to a greater extent) CFSR largely overestimate the median values of the observed  $Q_{LH}$ , indicating erroneously high cooling of the ocean surface. The significantly reduced bias in NHF from CFSR throughout all phases (Fig. 8t) indicates the systemic error in  $Q_{SW}$  is being largely compensated for by the systemic error in  $Q_{LH}$ . Hence, in the case of CFSR and (to much smaller extent) TropFlux, the erroneous strong cooling of the ocean surface from high  $Q_{LH}$  values offsets the erroneous high heating of the ocean surface from the  $Q_{SW}$  values. ERA-I generally captures the observed BSISO1  $Q_{net}$  variability; however, the  $Q_{SW}$  and  $Q_{LH}$  offsets add up and yield a  $Q_{net}$  of a sign opposite to the observed, consistent with Fig. 2.

ERA-I has a similar pattern of  $Q_{SW}$  and  $Q_{LH}$  biases, but the magnitude of errors is smaller in comparison to CFSR. The blended product, TropFlux, shows similar offsets in the  $Q_{SW}$ ; however, its  $Q_{LH}$  and  $Q_{net}$  is more realistic and appears to capture best the observed BSISO1  $Q_{SW}$  and  $Q_{LH}$

542 variability. These results are consistent with section 3, where it was showed that in general ERA-I  
543 does better at capturing radiative fluxes and TropFlux captures turbulent and net heat fluxes best.  
544 To calculate  $Q_{SW}$ , TropFlux uses observed cloudiness data from ISCCP up until 2009 (when it was  
545 last available), and the ISCCP mean seasonal cycle and NOAA OLR thereafter (KP12); while the  
546 four reanalysis products use their internally generated cloud fields, which are dependent on their  
547 convective and microphysical parameterization schemes. This highlights the well-known major  
548 errors in these schemes (e.g. Boilley and Wald 2015). These errors clearly impact intraseasonal  
549 variability as well as the mean fields.

550 Fig. 9 shows composites of daily anomalies from the monthly mean for the summer season  
551 (JJAS) from 2007 to 2015 for  $Q_{SW}$ ,  $Q_{LH}$ ,  $V$  and  $q_a$  during the most extreme phases, 2 and 5, of the  
552 BSISO1 life cycle over the BoB from TropFlux (shaded) and ERA-I (contour lines). During phase  
553 2, both products depict large positive  $Q_{SW}$  anomalies in the northern BoB, and negative  $Q_{LH}$  and  
554  $V$  anomalies in the eastern BoB (Fig. 9 a, b, c), indicating clear skies and suppressed convection  
555 in that region. In phase 5, the anomalies have flipped sign, and there is an elongated zonal band of  
556 negative  $Q_{SW}$  anomalies, and positive  $Q_{LH}$  and  $V$  anomalies across the BoB, indicating enhanced  
557 convection, in agreement with the BSISO1 life cycle from NOAA OLR and NCEP wind fields  
558 (Fig. 7) and the BSISO1 life cycle at the RAMA b28 location (Fig. 8). Generally, both TropFlux  
559 and ERA-I consistently capture the correct patterns of variability associated with the BSISO1 at  
560 phase 2 and 5 (see Fig. 7). However, ERA-I shows weaker  $Q_{SW}$  anomalies and stronger  $Q_{LH}$   
561 anomalies than TropFlux, consistent with results observed at the RAMA b28 location that suggest  
562 TropFlux is more accurate at this location (Fig. 8).

563 In contrast, the BSISO1 life cycles of  $Q_{SW}$  and  $Q_{LH}$  in JRA-55, MERRA-2 and CFSR are shown  
564 to be noisier (Fig. 10) than their counterparts in TropFlux and ERA-I, especially during phase 5.  
565 During phase 5, usually characterized by a zonal band of enhanced convection in the northern

BoB, JRA-55 only captures a weakened band of negative  $Q_{SW}$  anomalies in the northernmost and easternmost parts of the BoB (Fig. 10d). In MERRA-2, the BSISO1 signal is barely perceptible from the  $Q_{SW}$ , and in CFSR the band of  $Q_{SW}$  variability is weakened and shifted south (Fig. 10e, f). CFSR further shows exaggeratedly high positive  $Q_{LH}$  anomalies that compensate for the  $Q_{SW}$  bias. The diminished  $Q_{SW}$  variability in MERRA-2 can likely be attributed to the MERRA-2 negative bias, low correlation and poor skill score in  $Q_{SW}$  (Fig. 2). The difficulties of MERRA-2, JRA-55 and CFSR in capturing the BSISO1 signal across the basin is consistent with their difficulties capturing the BSISO1 variability at RAMA b28 (Fig. 8) and can be directly attributed to the products difficulties in representing surface fluxes, as seen in the previous sections (i.e. section 3, 4). In general, TropFlux and ERA-I captured the observed BSISO1  $Q_{SW}$  best, and TropFlux captured the observed BSISO1  $Q_{LH}$  and  $Q_{net}$  best; both products depicted a life cycle composite which was encouragingly similar to the Lee et al. (2013) OLR life cycle (Fig. 8).

Finally, we note that with low wind speeds and high radiation, the effectiveness of the radiation shields on the  $T_a$  and humidity sensor decreases (Anderson and Baumgartner 1998). Anderson and Baumgartner (1998) estimated that for naturally ventilated sensors, errors of up to  $3.4^\circ\text{C}$  in the mean daytime temperature could lead to biases of  $22\text{ W m}^{-2}$  in the turbulent fluxes. Here the  $T_a$  and humidity sensor aboard the ATLAS moorings used multi-plate radiation shield and are naturally ventilated, hence high radiation and low wind speeds may result in less effective radiation shields (Freitag et al. 2001). Specifically, manufacturer estimates that for radiation above  $1080\text{ W m}^{-2}$  and winds at or below  $3\text{ m s}^{-1}$ , the temperature bias can increase from  $0.2^\circ\text{C}$  to  $0.4^\circ\text{C}$  (Freitag et al. 2001). During phase 1 of the BSISO1, when wind speeds drop to  $3\text{ m s}^{-1}$  and the solar radiation is quite high due to suppressed convection, there are greater chances of  $T_a$  errors occurring due to failing radiation shields. However, careful examination of the  $T_a$  anomalies per phase (not shown here) suggests there are no significant  $T_a$  errors. The high wind speed during the

majority of the phases (2 through 8) decreases the chances of radiation shields contributing to the overall error.

## 6. Summary and Conclusions

In this study, five data products are analysed and compared with in situ data from a moored array in the BoB to determine how well the reanalysis products characterise air-sea fluxes and intraseasonal variability during the SW monsoon season. Specifically, meteorological parameters,  $SST$ ,  $V$ ,  $T_a$  and  $q_a$ , air-sea temperature difference,  $\Delta T$ , air-sea humidity difference,  $\Delta q$ , and fluxes,  $Q_{SW}$ ,  $Q_{LW}$ ,  $Q_{SH}$ ,  $Q_{LH}$  and  $Q_{net}$  from ERA-I, TropFlux, JRA-55, MERRA-2 and CFSR were evaluated for JJAS from 2007–2015, and compared with in situ data from the RAMA surface flux reference site at  $15^\circ\text{N}$ ,  $90^\circ\text{E}$ , denoted b28. In general, most products did reasonably well at representing the meteorological variables, though  $q_a$  had the lowest correlations, highest biases and lowest skill scores across all products (Fig. 2). TropFlux and ERA-I performed best, while the coupled product, CFSR, exhibited some of the largest biases. From the flux variables,  $Q_{SW}$  and  $Q_{LH}$  were shown to be the main drivers of the observed  $Q_{net}$  variability, but were also the two variables the products had the most difficulty capturing. Correlations were lowest for the radiative fluxes and  $Q_{SH}$ , and there were non-negligible biases in the range of  $50 \text{ W m}^{-2}$  in  $Q_{SW}$ . For  $Q_{LH}$ , all products other than TropFlux overestimated the observed  $Q_{LH}$  by at least  $40 \text{ W m}^{-2}$ , while the TropFlux bias was  $\sim 10 \text{ W m}^{-2}$ . In general, based on mean biases, correlations and skill scores, ERA-I was shown to capture radiative fluxes best, while TropFlux better captured turbulent and latent heat fluxes. Skill scores indicated poor performance for  $Q_{LH}$  and the radiative fluxes in MERRA-2 and CFSR, and we note that for the coupled ocean-atmosphere product CFSR, these biases canceled each other out in the  $Q_{net}$ .

612 The temporal mean fields for the fluxes across the BoB were investigated in section 5a, where  
 613 various discrepancies were observed in the spatial patterns among the products. For  $Q_{SH}$ , the  
 614 patterns were consistent across ERA-I, TropFlux and CFSR, though JRA-55 and ERA-I had large  
 615 negative biases, indicating erroneously high heat loss to the atmosphere and therefore erroneous  
 616 cooling of the sea surface. Patterns of  $Q_{LH}$  variability were generally consistent across all products  
 617 (i.e. a region of high  $Q_{LH}$  in the southwest corner of the BoB), though values ranged on the order  
 618 of  $40 \text{ W m}^{-2}$  between the reanalysis products. For  $Q_{SW}$ , ERA-I outperformed the other three  
 619 products by a wide margin (CFSR, in particular, showed much higher values and different spatial  
 620 gradients than the other products). Differences in  $Q_{LH}$  and  $Q_{SW}$  in the reanalysis products were  
 621 generally attributed to differences or issues with the internally-generated cloud fields/schemes (e.g.  
 622 Wang et al. 2011; Boilley and Wald 2015). For  $Q_{LW}$ , though spatial gradients were consistent,  
 623 correlations high and biases small, skill scores were low (except for ERA-I) across all products. In  
 624 general, results from the temporal mean field indicate results at the b28 location are not localized,  
 625 and biases of similar magnitude to those seen at b28 will be widespread across the BoB. Further,  
 626 the biases in the fluxes implied by the meteorological parameters at b28 are likely representative of  
 627 the magnitude of biases observed in other regions in the basin, in the temporally-averaged fields.

628 The BSISO1 index, representative of the northward propagating component of the summer mon-  
 629 soon (with a 30–60 day periodicity), was used to test the ability of the different products to rep-  
 630 resent the principal mode of atmospheric variability in the BoB in this season, in particular in  
 631 the representation of  $Q_{SW}$  and  $Q_{LH}$  in ERA-I, TropFlux, and CFSR. Comparison with RAMA  
 632 b28 suggested TropFlux and ERA-I most reliably captured surface flux variability compared with  
 633 the observed BSISO1  $Q_{SW}$  cycle at  $15^\circ\text{N}$ ,  $90^\circ\text{E}$ ; however, TropFlux captured the variability and  
 634 magnitude of the observed  $Q_{LH}$  and  $Q_{net}$  best. The analysis of the mean fields, the comparison  
 635 with BSISO1 at b28, and comparison with Lee et al. (2013) satellite OLR maps allows us to ex-

636 tend this confidence over the entire BoB. Thus, both TropFlux and ERA-I appear to best represent  
637 the variability of the surface fluxes at RAMA b28 and across the entire BoB basin. Conversely,  
638 MERRA-2, CFSR and JRA-55 struggled to capture the climatic variability associated with the  
639 BSISO1, with weak  $Q_{SW}$  variability at the location of RAMA b28 suggesting that the convective  
640 signal is poorly represented in these products, while the over-estimation of  $Q_{LH}$  variability sug-  
641 gests erroneous surface wind and humidity fields. Hence, we infer inability to accurately capture  
642 or reproduce the surface fluxes at b28 or at mean field levels shows that the MERRA-2, CFSR and  
643 JRA-55 products will similarly struggle to capture variability associated with the boreal summer  
644 monsoon.

645 As air-sea fluxes have been shown to be key players in monsoon variability (Vecchi and Har-  
646 rison 2002), caution is advised when selecting a data product to represent monsoonal processes.  
647 This study has highlighted significant and critical deficiencies in reanalysis flux products from  
648 the accumulated errors observed in the meteorological parameters and surface fluxes specific to  
649 the southwest monsoon time period and have yet to be verified for the entire seasonal cycle. In  
650 general, ERA-I and TropFlux were shown to outperform MERRA-2, JRA-55 and CFSR; ERA-  
651 I represented radiative fluxes best, while TropFlux better captured turbulent and net heat fluxes.  
652 Based on findings shown here, this analysis recommends TropFlux and ERA-I as the best available  
653 products for the study of air-sea fluxes and intraseasonal variability over the BoB during the SW  
654 monsoon, or for the forcing of ocean models during boreal summer in the tropical Indian Ocean.

655 *Acknowledgments.* The NERC BoBBLE project supported ASF and ECK (NE/L013835/1),  
656 BGMW (NE/L013827/1), and SCP (NE/L013800/1). PNV thanks the Ministry of Earth  
657 Sciences, Govt. of India for funding under the BoBBLE project. The authors thank  
658 the US National Oceanic and Atmospheric Administration (NOAA)/Pacific Marine Environ-

659 mental Laboratory (PMEL) and National Institute of Oceanography (NIO) for access to  
660 RAMA buoy data (<https://www.pmel.noaa.gov/tao/drupal/disdel/>). The authors would also  
661 like to acknowledge the European Centre for Medium Range Weather Forecasting for ERA-  
662 Interim data access (<http://apps.ecmwf.int/datasets/data/interim-full-daily/levtype=pl/>); the Com-  
663 putational and Information Systems Laboratory Research Data Archive (<https://rda.ucar.edu>)  
664 for access to the reanalysis datasets JRA-55 and CFSR; the Global Modeling and As-  
665 simulation Office (GMAO) and the GES DISC for the dissemination of MERRA-2  
666 (<https://disc.sci.gsfc.nasa.gov/daac-bin/FTPSubset2.pl>); and, ESSO-INCOIS for TropFlux data  
667 access (<http://www.incois.gov.in/tropflux/>). The TropFlux data is produced under a collab-  
668 oration between Laboratoire d’Oceanographie: Experimentation et Approches Numeriques  
669 (L’OCEAN) from Institut Pierre Simon Laplace (IPSL, Paris, France) and National Insti-  
670 tute of Oceanography/CSIR (NIO, Goa, India), and supported by Institut de Recherche pour  
671 le Developpement (IRD, France). TropFlux relies on data provided by the ECMWF Re-  
672 Analysis interim (ERA-I) and ISCCP projects. The interpolated OLR and NCEP Reanalysis  
673 data were provided by the NOAA/OAR/ESRL PSD, Boulder, Colorado, USA, from their web  
674 site at <http://www.cdc.noaa.gov/>. The BSISO data were provided by the Apec Climate Cen-  
675 tre through their website: <http://www.apcc21.net/ser/moni.do?lang=en>. The authors are grate-  
676 ful to Dr. Shoji Hirahara of JMA for the JRA-55 daily SST data. The matlab version of  
677 the COARE3.0 algorithm was used to estimate the uncertainty in the RAMA turbulent fluxes:  
678 <ftp://ftp.etl.noaa.gov/BLO/Air-Sea/bulkalg/cor3.0/>. The authors are also grateful for the helpful  
679 insight and comments from three anonymous reviewers.



## References

- Anderson, S. P., and M. F. Baumgartner, 1998: Radiative Heating Errors in Naturally Ventilated Air Temperature Measurements Made from Buoys. *Journal of Atmospheric and Oceanic Technology*, **15** (1), 157–173.
- Berrisford, P., P. Kållberg, S. Kobayashi, D. Dee, S. Uppala, A. J. Simmons, P. Poli, and H. Sato, 2011: Atmospheric conservation properties in ERA-Interim. *Quarterly Journal of the Royal Meteorological Society*, **137** (659), 1381–1399, doi:10.1002/qj.864.
- Boilley, A., and L. Wald, 2015: Comparison between meteorological re-analyses from ERA-Interim and MERRA and measurements of daily solar irradiation at surface. *Renewable Energy*, **75**, 135–143, doi:10.1016/j.renene.2014.09.042.
- Bolker, B. M., 2008: *Ecological models and data in R*. Princeton University Press, 508 pp.
- Bolton, D., 1980: The computation of equivalent potential temperature. *Monthly weather review*, **108** (7), 1046–1053, doi:10.1175/1520-0493(1980)108<1046:TCOEPT>2.0.CO;2.
- Bosilovich, M. G., and Coauthors, 2015: MERRA-2: Initial Evaluation of the Climate. *Series on Global Modeling and Data Assimilation, NASA/TM*, **43** (104606), 1–139.
- Brunke, M. A., Z. Wang, X. Zeng, M. Bosilovich, and C. Shie, 2011: An assessment of the uncertainties in ocean surface turbulent fluxes in 11 reanalysis, satellite-derived, and combined global datasets. *Journal of Climate*, **24** (21), 5469–5493.
- Cronin, M. F., C. W. Fairall, and M. J. McPhaden, 2006: An assessment of buoy-derived and numerical weather prediction surface heat fluxes in the tropical Pacific. *Journal of Geophysical Research: Oceans*, **111** (C6), doi:10.1029/2005JC003324.

701 Dee, D. P., and S. Uppala, 2009: Variational bias correction of satellite radiance data in the ERA-  
 702 Interim reanalysis. *Quarterly Journal of the Royal Meteorological Society*, **135 (644)**, 1830–  
 703 1841, doi:10.1002/qj.493.

704 Dee, D. P., and Coauthors, 2011: The ERA-Interim reanalysis: Configuration and performance of  
 705 the data assimilation system. *Quarterly Journal of the Royal Meteorological Society*, **137 (656)**,  
 706 553–597, doi:10.1002/qj.828.

707 DeMott, C. A., C. Stan, D. A. Randall, and M. D. Branson, 2014: Intraseasonal Variability in Cou-  
 708 pled GCMs: The Roles of Ocean Feedbacks and Model Physics. *Journal of Climate*, **27 (13)**,  
 709 4970–4995, doi:10.1175/JCLI-D-13-00760.1.

710 Donlon, C. J., M. Martin, J. Stark, J. Roberts-Jones, E. Fiedler, and W. Wimmer, 2012: The  
 711 Operational Sea Surface Temperature and Sea Ice Analysis (OSTIA) system. *Remote Sensing*  
 712 *of Environment*, **116**, 140–158, doi:10.1016/j.rse.2010.10.017.

713 Duncan, B., and W. Han, 2009: Indian Ocean intraseasonal sea surface temperature variability  
 714 during boreal summer: Madden-Julian Oscillation versus submonthly forcing and processes.  
 715 *Journal of Geophysical Research: Oceans*, **114 (5)**, doi:10.1029/2008JC004958.

716 Fairall, C. W., E. F. Bradley, J. E. Hare, A. A. Grachev, and J. B. Edson, 2003: Bulk parameteriza-  
 717 tion of air-sea fluxes: Updates and verification for the COARE algorithm. *Journal of Climate*,  
 718 **16 (4)**, 571–591, doi:10.1175/1520-0442(2003)016<0571:BPOASF>2.0.CO;2.

719 Freitag, H. P., M. OHaleck, G. Thomas, and M. McPhaden, 2001: Calibration procedures and  
 720 instrumental accuracies for ATLAS wind measurements. *NOAA Tech. Memo. OAR PMEL*, **119**,  
 721 20.

722 Girishkumar, M. S., J. Joseph, V. P. Thangaprakash, V. Pottapinjara, and M. J. McPhaden, 2017:  
 723 Mixed Layer Temperature Budget for the Northward Propagating Summer Monsoon Intrasea-  
 724 sonal Oscillation (MISO) in the Central Bay of Bengal. *Journal of Geophysical Research:*  
 725 *Oceans*, **122** (11), 8841–8854.

726 Goswami, B. B., M. Deshpande, P. Mukhopadhyay, S. K. Saha, S. A. Rao, R. Murthugudde,  
 727 and B. N. Goswami, 2014: Simulation of monsoon intraseasonal variability in NCEP CFSv2  
 728 and its role on systematic bias. *Climate Dynamics*, **43** (9-10), 2725–2745, doi:10.1007/  
 729 s00382-014-2089-5.

730 Ishii, M., A. Shouji, S. Sugimoto, and T. Matsumoto, 2005: Objective analyses of sea-surface  
 731 temperature and marine meteorological variables for the 20th century using ICOADS and the  
 732 Kobe Collection. *International Journal of Climatology*, **25** (7), 865–879, doi:10.1002/joc.1169.

733 Kikuchi, K., and B. Wang, 2010: Formation of Tropical Cyclones in the Northern Indian Ocean  
 734 Associated with Two Types of Tropical Intraseasonal Oscillation Modes. *Journal of the Meteoro-*  
 735 *logical Society of Japan*, **88** (3), 475–496, doi:10.2151/jmsj.2010-313.

736 Kobayashi, S., and Coauthors, 2015: The JRA-55 Reanalysis: General Specifications and Basic  
 737 Characteristics. *Journal of the Meteorological Society of Japan. Ser. II*, **93** (1), 5–48, doi:10.  
 738 2151/jmsj.2015-001.

739 Kumar, B. P., J. Vialard, M. Lengaigne, and M. J. Mcphaden, 2012: TropFlux: Air-Sea Fluxes for  
 740 the Global Tropical Oceans Description and evaluation against observations. *Climate Dynam-*  
 741 *ics*, **38** (7), 1521–1543, doi:10.1007/s00382-011-1115-0.

742 Lau, W. K. M., D. E. Waliser, and B. N. Goswami, 2012: South Asian monsoon. *Intraseasonal*  
 743 *variability in the atmosphere-ocean climate system*, Springer Berlin Heidelberg, 21–72.

- 744 Lee, J. Y., B. Wang, M. C. Wheeler, X. Fu, D. E. Waliser, and I. S. Kang, 2013: Real-time  
745 multivariate indices for the boreal summer intraseasonal oscillation over the Asian summer  
746 monsoon region. *Climate Dynamics*, **40** (1-2), 493–509, doi:10.1007/s00382-012-1544-4.
- 747 McPhaden, M., 2010: The Global Tropical Moored Buoy Array. *Proceedings of OceanObs'09:  
748 Sustained Ocean Observations and Information for Society*, **9** (1), 668–682, doi:10.5270/  
749 OceanObs09.cwp.61.
- 750 McPhaden, M. J., and Coauthors, 2009: RAMA: The research moored array for African-Asian-  
751 Australian monsoon analysis and prediction. *Bulletin of the American Meteorological Society*,  
752 **90** (4), 459–480, doi:10.1175/2008BAMS2608.1.
- 753 Murphy, A. H., 1988: Skill Scores Based on the Mean Square Error and Their Relationships  
754 to the Correlation Coefficient. *Monthly Weather Review*, **116** (12), 2417–2424, doi:10.1175/  
755 1520-0493(1988)116<2417:SSBOTM>2.0.CO;2.
- 756 Onogi, K., and Coauthors, 2007: The JRA-25 reanalysis. *Journal of the Meteorological Society of  
757 Japan. Ser. II*, **85** (3), 369–432, doi:10.2151/jmsj.85.369.
- 758 Parampil, S. R., A. Gera, M. Ravichandran, and D. Sengupta, 2010: Intraseasonal response of  
759 mixed layer temperature and salinity in the Bay of Bengal to heat and freshwater flux. *Journal  
760 of Geophysical Research: Oceans*, **115** (5), doi:10.1029/2009JC005790.
- 761 Puvaneswaran, K. M., and P. A. Smithson, 1991: Precipitation elevation relationships over Sri  
762 Lanka. *Theoretical and Applied Climatology*, **43** (3), 113–122, doi:10.1007/BF00867468.
- 763 R Core Team, 2015: R: A Language and Environment for Statistical Computing. URL [http://www.](http://www.r-project.org/)  
764 [r-project.org/](http://www.r-project.org/), {ISBN} 3–900051–07–0 pp., doi:ISBN3-900051-07-0, /www.R-project.org.

765 Rienecker, M., and Coauthors, 2011: MERRA-NASA's Modern-Era Retrospective Analysis for  
 766 Research and Applications. *Bulletin of the American Meteorological Society*, **24 (14)**, 3624–  
 767 3648, doi:10.1175/JCLI-D-11-00015.1.

768 Saha, S., and Coauthors, 2010: The NCEP climate forecast system reanalysis. *Bulletin of*  
 769 *the American Meteorological Society*, **91 (8)**, 1015–1057, doi:10.1175/2010BAMS3001.1,  
 770 9809069v1.

771 Saha, S., and Coauthors, 2011: NCEP Climate Forecast System Version 2 (CFSv2) 6-hourly Prod-  
 772 ucts. URL <http://dx.doi.org/10.5065/D61C1TXF>, doi:10.5065/D61C1TXF.

773 Schiller, A., and J. Godfrey, 2003: Indian Ocean intraseasonal variability in an ocean general cir-  
 774 culation model. *Journal of Climate*, **16 (1999)**, 21–39, doi:10.1175/1520-0442(2003)016<0021:  
 775 IOIVIA>2.0.CO;2.

776 Sengupta, D., and M. Ravichandan, 2001: Oscillations of the Bay of Bengal SST during the 1998  
 777 summer monsoon. *Geophys. Res. Lett.*, **28 (10)**, 2033–2036, doi:10.1029/2000GL012548.

778 Sikka, D. R., and S. Gadgil, 1980: On the Maximum Cloud Zone and the ITCZ over Indian,  
 779 Longitudes during the Southwest Monsoon. *Monthly Weather Review*, **108 (11)**, 1840–1853,  
 780 doi:10.1175/1520-0493(1980)108<1840:OTMCZA>2.0.CO;2.

781 Suhas, E., J. M. Neena, and B. N. Goswami, 2013: An Indian monsoon intraseasonal oscillations  
 782 (MISO) index for real time monitoring and forecast verification. *Climate Dynamics*, **40 (11)**,  
 783 2605–2616, doi:10.1007/s00382-012-1462-5.

784 Vecchi, G. A., and D. E. Harrison, 2002: Monsoon breaks and subseasonal sea surface tem-  
 785 perature variability in the Bay of Bengal. *Journal of Climate*, **15 (12)**, 1485–1493, doi:  
 786 10.1175/1520-0442(2002)015<1485:MBASSS>2.0.CO;2.

787 Vialard, J., A. Jayakumar, C. Gnanaseelan, M. Lengaigne, D. Sengupta, and B. N. Goswami, 2011:  
788 Processes of 3090 days sea surface temperature variability in the northern Indian Ocean during  
789 boreal summer. *Climate Dynamics*, **38 (9-10)**, 1901–1916, doi:10.1007/s00382-011-1015-3.

790 Vinayachandran, P. N., V. S. N. Murty, and V. R. Babu, 2002: Observations of barrier layer forma-  
791 tion in the Bay of Bengal during summer monsoon. *Journal of Geophysical Research: Oceans*,  
792 **107 (C12)**, 2156–2202, doi:10.1029/2001JC000831.

793 Vinayachandran, P. N., and Coauthors, 2018: BoBBLE (Bay of Bengal Boundary Layer Experi-  
794 ment): Ocean-atmosphere interaction and its impact on the South Asian monsoon. *Bulletin of*  
795 *the American Meteorological Society*, doi:10.1175/BAMS-D-16-0230.1.

796 Waliser, D. E., 2006: Intraseasonal variability. *The Asian Monsoon*, Springer Berlin Heidelberg,  
797 Berlin, 203–257, doi:10.1007/3-540-37722-0\_5.

798 Wallcraft, A. J., A. B. Kara, C. N. Barron, E. J. Metzger, R. L. Pauley, and M. A. Bourassa,  
799 2009: Comparisons of monthly mean 10 m wind speeds from satellites and NWP products  
800 over the global ocean. *Journal of Geophysical Research Atmospheres*, **114 (16)**, doi:10.1029/  
801 2008JD011696.

802 Wang, B., P. J. Webster, and H. Teng, 2005: Antecedents and self-induction of active-break south  
803 Asian monsoon unraveled by satellites. *Geophysical Research Letters*, **32 (4)**, 1–4, doi:10.1029/  
804 2004GL020996.

805 Wang, W., P. Xie, S. H. Yoo, Y. Xue, A. Kumar, and X. Wu, 2011: An assessment of the surface  
806 climate in the NCEP climate forecast system reanalysis. *Climate Dynamics*, **37 (7-8)**, 1601–  
807 1620, doi:10.1007/s00382-010-0935-7.

808 Webster, P. J., V. O. Magaña, T. N. Palmer, J. Shukla, R. A. Tomas, M. Yanai, and T. Yasunari,  
 809 1998: Monsoons: Processes, predictability, and the prospects for prediction. *Journal of Geo-*  
 810 *physical Research: Oceans*, **103 (C7)**, 14 451–14 510, doi:10.1029/97JC02719, 0402594v3.

811 Weller, R., and Coauthors, 2016: Air-Sea Interaction in the Bay of Bengal. *Oceanography*, **29 (2)**,  
 812 28–37, doi:10.5670/oceanog.2016.36.

813 Wheeler, M. C., and H. H. Hendon, 2004: An All-Season Real-Time Multivariate MJO Index:  
 814 Development of an Index for Monitoring and Prediction. *Monthly Weather Review*, **132 (8)**,  
 815 1917–1932, doi:10.1175/1520-0493(2004)132(1917:AARMMI)2.0.CO;2, arXiv:1011.1669v3.

816 Xue, Y., B. Huang, Z. Z. Hu, A. Kumar, C. Wen, D. Behringer, and S. Nadiga, 2011: An assess-  
 817 ment of oceanic variability in the NCEP climate forecast system reanalysis. *Climate Dynamics*,  
 818 **37 (11-12)**, 2511–2539, doi:10.1007/s00382-010-0954-4.

819 Yang, B., X. Fu, and B. Wang, 2008: Atmosphere-ocean conditions jointly guide convection of  
 820 the Boreal Summer Intraseasonal Oscillation: Satellite observations. *Journal of Geophysical*  
 821 *Research Atmospheres*, **113 (11)**, doi:10.1029/2007JD009276.

822 Yu, L., X. Jin, and R. A. Weller, 2007: Annual, Seasonal, and Interannual Variability of  
 823 AirSea Heat Fluxes in the Indian Ocean. *Journal of Climate*, **20 (13)**, 3190–3209, doi:  
 824 10.1175/JCLI4163.1.

825 Zhang, Y., W. B. Rossow, A. A. Lacis, V. Oinas, and M. I. Mishchenko, 2004: Calculation of  
 826 radiative fluxes from the surface to top of atmosphere based on ISCCP and other global data  
 827 sets: Refinements of the radiative transfer model and the input data. *Journal of Geophysical*  
 828 *Research D: Atmospheres*, **109 (19)**, doi:10.1029/2003JD004457.

829	<b>LIST OF TABLES</b>	
830	<b>Table 1.</b> Summary of reanalysis, blended* and in situ products used in this study. . . . .	39
831	<b>Table 2.</b> Summary of documented ( $SST$ , $V$ , $T_a$ , and $q_a$ ) uncertainties (McPhaden et al.	
832	2009) and calculated ( $\Delta T$ , $\Delta q$ , $Q_{SH}$ , and $Q_{LH}$ ) uncertainties from the RAMA	
833	buoy instruments. . . . .	40



TABLE 1. Summary of reanalysis, blended\* and in situ products used in this study.

<i>Product</i>	<i>Input SST</i>	<i>Resolution</i>	<i>Period</i>	<i>Reference</i>	<i>Flux method</i>
ERA-Interim	See Dee et al. (2011)	-Sub-daily (3, 6-hourly) -0.75° X 0.75°	1979 to present	Dee et al. (2011)	Model
TropFlux*	Bias corrected ERA-I	-Daily -1.0° X 1.0°	1979 to present	Kumar et al. (2012)	COARE 3.0
JRA-55	COBE SST (Ishii et al. 2005)	-Sub-daily (3, 6-hourly) -0.56° X 0.56°	1979 to present	Kobayashi et al. (2015)	Model
MERRA-2	See Bosilovich et al. (2015)	-Sub-daily (1-hourly) -0.5° X 0.625°	1980 to present	Bosilovich et al. (2015)	Model
CFSR	See Saha et al. (2011)	-Sub-daily (6-hourly) -0.5° X 0.5°	1979 to 2011 CFSv2: 2011 to pres.	Saha et al. (2010) Saha et al. (2011)	Model
RAMA array	Observed	-Sub-daily (1-hourly fluxes; 2-min radiation data; 10-min surface meteorological data)	2007 to present	McPhaden et al. (2009)	COARE 3.0

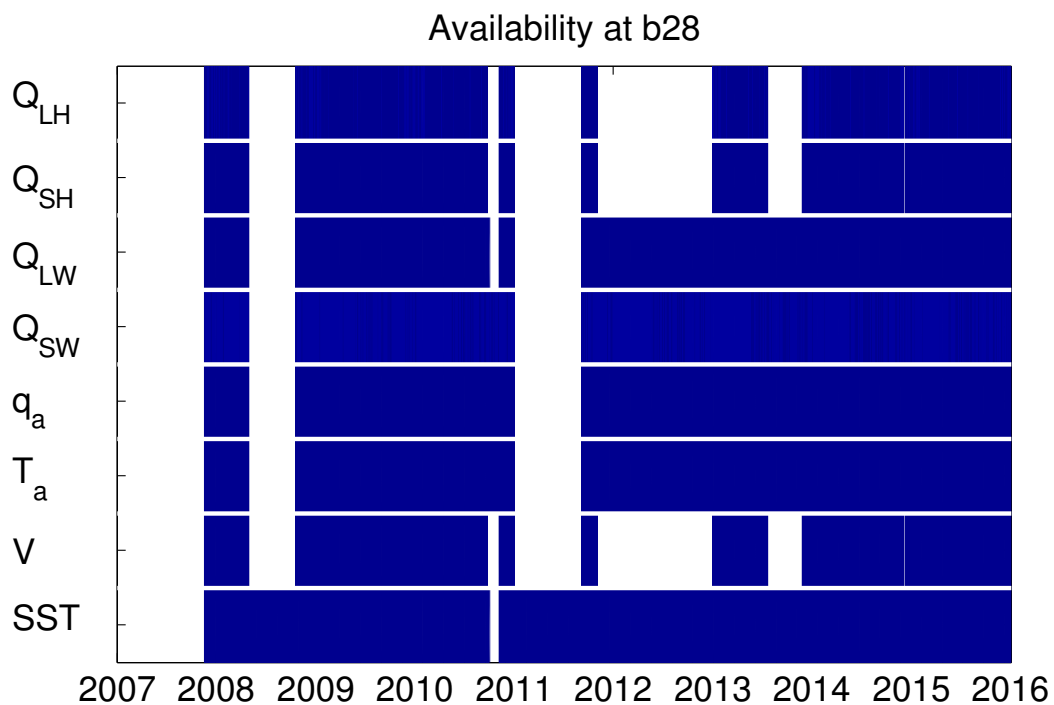
834 TABLE 2. Summary of documented ( $SST$ ,  $V$ ,  $T_a$ , and  $q_a$ ) uncertainties (McPhaden et al. 2009) and calculated  
835 ( $\Delta T$ ,  $\Delta q$ ,  $Q_{SH}$ , and  $Q_{LH}$ ) uncertainties from the RAMA buoy instruments.

<i>Measurement</i>	<i>Uncertainty</i>
$SST$	$\pm 0.02^\circ C$
$V$	$\pm 0.2 \text{ m s}^{-1}$
$T_a$	$\pm 0.2^\circ C$
$q_a$	$\pm 0.2 \text{ g kg}^{-1}$
$\Delta T$	$\pm 0.2^\circ C$
$\Delta q$	$\pm 0.28 \text{ g kg}^{-1}$
$Q_{SH}$	$\pm 2.5 \text{ W m}^{-2}$
$Q_{LH}$	$\pm 7.3 \text{ W m}^{-2}$

## LIST OF FIGURES

<b>Fig. 1.</b>	Availability of data at buoy site b28 (15°N and 90°E b28) for meteorological and flux parameters used in this study. . . . .	43
<b>Fig. 2.</b>	Difference (product - RAMA; a), correlation (b), variance ratio (c), and skill score (d) for reanalysis products (ERA-I, TropFlux, JRA-55, MERRA-2 and CFSR) against data from RAMA b28. The 95% confidence intervals are shown in the difference, correlation and variance ratio metrics. The variables evaluated are the meteorological, SST (°C), $V$ (m s <sup>-1</sup> ), $T_a$ (°C), $q_a$ (g kg <sup>-1</sup> ), $\Delta T$ (°C), $\Delta q$ (g kg <sup>-1</sup> ), and flux, $Q_{SW}$ (W m <sup>-2</sup> ), $Q_{LW}$ (W m <sup>-2</sup> ), $Q_{SH}$ (W m <sup>-2</sup> ), $Q_{LH}$ (W m <sup>-2</sup> ), $Q_{net}$ (W m <sup>-2</sup> ), for the summer (JJAS) from 2007 to 2015. Panel (a) shows uncertainties as per Table 2 indicated by the horizontal dashed lines, and a split scale to differentiate between meteorological and flux parameters. . . . .	44
<b>Fig. 3.</b>	Scatterplots for $Q_{net}$ vs each of $Q_{SW}$ , $Q_{LW}$ , $Q_{SH}$ and $Q_{LH}$ (all units in W m <sup>-2</sup> ) from RAMA buoy observations (a, b, c, d), ERA-I (e, f, g, h), TropFlux (i, j, k, l), JRA-55 (m, n, o, p), MERRA-2 (q, r, s, t) and CFSR (u, v, w, x) at site b28 (8°N and 90°E). Contour lines enclose the 10% and 50% of points in each joint distribution. RAMA contour lines (black) are repeated for comparison. . . . .	45
<b>Fig. 4.</b>	Scatterplots of $Q_{LH}$ (W m <sup>-2</sup> ) vs $\Delta q$ (g kg <sup>-1</sup> ), $Q_{LH}$ (W m <sup>-2</sup> ) vs $V$ (m s <sup>-1</sup> ), $\Delta q$ (g kg <sup>-1</sup> ) vs $V$ (m s <sup>-1</sup> ), $Q_{SH}$ (W m <sup>-2</sup> ) vs $\Delta T$ (°C), $Q_{SH}$ (W m <sup>-2</sup> ) vs $V$ (m s <sup>-1</sup> ), $\Delta T$ (°C) vs $V$ (m s <sup>-1</sup> ), and $Q_{LW}$ (W m <sup>-2</sup> ) vs $Q_{SW}$ (W m <sup>-2</sup> ) from RAMA buoy observations (left column), ERA-Interim (center column) and TropFlux (right column) at site b28 (8°N and 90°E). Contour lines enclose the 10% and 50% of points in each joint distribution. RAMA contour lines (black) are repeated for comparison. . . . .	46
<b>Fig. 5.</b>	Mean $Q_{SH}$ (left column; W m <sup>-2</sup> ) and $Q_{LH}$ (right column; W m <sup>-2</sup> ) for ERA-I (a, f), TropFlux (b, g), JRA-55 (c, h), MERRA-2 (d, i), and CFSR (e, j). All fields are averaged for the SW monsoon season (JJAS) from 2007 to 2015. The black square indicates the location of the RAMA buoy, b28, in the Bay of Bengal. . . . .	47
<b>Fig. 6.</b>	Same as in Fig. 5 but for radiative fluxes. . . . .	48
<b>Fig. 7.</b>	BSISO 1 life cycle composite of NOAA OLR anomalies (shaded; W m <sup>-2</sup> ) and NCEP-DOE 850-hPa wind anomalies (vector; m s <sup>-1</sup> ). . . . .	49
<b>Fig. 8.</b>	Median, interquartile range, 95% confidence interval, and outliers for $V$ (m s <sup>-1</sup> ), wind direction (°), $Q_{SW}$ (W m <sup>-2</sup> ), $Q_{LH}$ (W m <sup>-2</sup> ), and $Q_{net}$ (W m <sup>-2</sup> ) vs BSISO1 phases (1 to 8) from RAMA b28 (a, e, i, m, q), ERA-I (b, f, j, n, r), TropFlux (c, g, k, o, s), and CFSR (d, h, l, p, t). The red line is the RAMA b28 median line, repeated for comparison. . . . .	50
<b>Fig. 9.</b>	Composite of phase 2 (left column) and phase 5 (right column) of the BSISO1 life cycle. TropFlux (shaded) and ERA-I (contour lines) $Q_{SW}$ anomalies at phase 2 (a) and phase 5 (e); $Q_{LH}$ anomalies at phase 2 (b) and 5 (f); $V$ anomalies at phase 2 (c) and 5 (g); and, $q_a$ anomalies at phase 2 (d) and 5 (h). ERA-I $Q_{SW}$ contour lines range from -40 to 40 W m <sup>-2</sup> and $Q_{LH}$ contour lines range from -30 to 30 W m <sup>-2</sup> , with 5 W m <sup>-2</sup> intervals. ERA-I $V$ contour lines range from -3 to 3 m s <sup>-1</sup> , with 0.5 m s <sup>-1</sup> intervals. ERA-I $q_a$ contour lines range from -1 to 1 g kg <sup>-1</sup> , with 0.2 g kg <sup>-1</sup> intervals. The black square indicates the location of the RAMA buoy 28. . . . .	51
<b>Fig. 10.</b>	Phase 2 (left column) and 5 (right column) of the $Q_{SW}$ (shading) and $Q_{LH}$ (contour line) anomalies from JRA-55 (a, d), MERRA-2 (b, e), and CFSR (c, f) based on the BSISO1	

879 phases.  $Q_{LH}$  contour lines range from -40 to 40  $\text{W m}^{-2}$ , with 5  $\text{W m}^{-2}$  intervals. The black  
880 square indicates the location of the RAMA buoy 28. All units in  $\text{W m}^{-2}$ . . . . . 52



881 FIG. 1. Availability of data at buoy site b28 (15°N and 90°E b28) for meteorological and flux parameters  
882 used in this study.

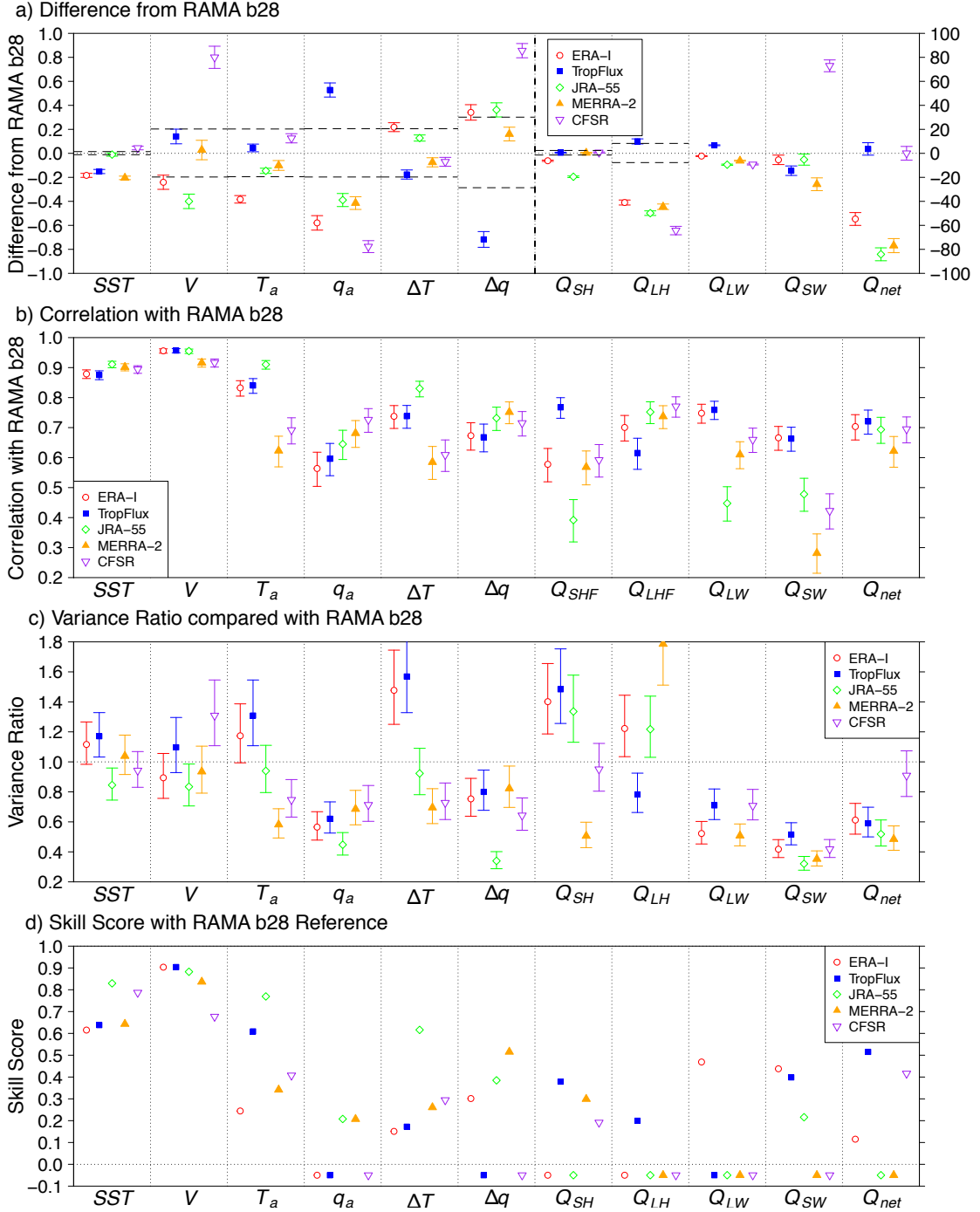


FIG. 2. Difference (product - RAMA; a), correlation (b), variance ratio (c), and skill score (d) for reanalysis products (ERA-I, TropFlux, JRA-55, MERRA-2 and CFSR) against data from RAMA b28. The 95% confidence intervals are shown in the difference, correlation and variance ratio metrics. The variables evaluated are the meteorological, SST ( $^{\circ}\text{C}$ ),  $V$  ( $\text{m s}^{-1}$ ),  $T_a$  ( $^{\circ}\text{C}$ ),  $q_a$  ( $\text{g kg}^{-1}$ ),  $\Delta T$  ( $^{\circ}\text{C}$ ),  $\Delta q$  ( $\text{g kg}^{-1}$ ), and flux,  $Q_{SW}$  ( $\text{W m}^{-2}$ ),  $Q_{LW}$  ( $\text{W m}^{-2}$ ),  $Q_{SH}$  ( $\text{W m}^{-2}$ ),  $Q_{LH}$  ( $\text{W m}^{-2}$ ),  $Q_{net}$  ( $\text{W m}^{-2}$ ), for the summer (JJAS) from 2007 to 2015. Panel (a) shows uncertainties as per Table 2 indicated by the horizontal dashed lines, and a split scale to differentiate between meteorological and flux parameters.

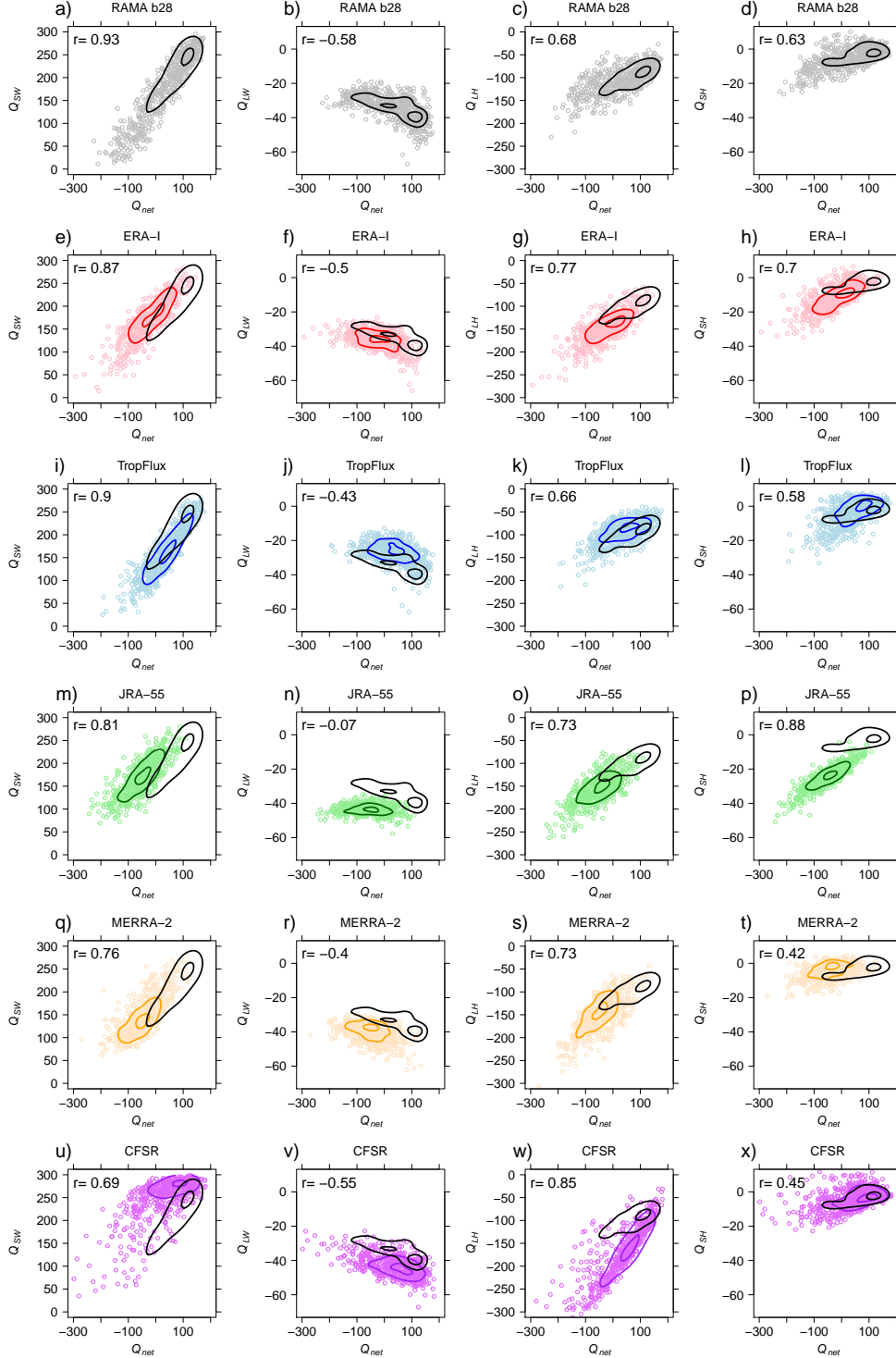


FIG. 3. Scatterplots for  $Q_{net}$  vs each of  $Q_{SW}$ ,  $Q_{LW}$ ,  $Q_{SH}$  and  $Q_{LH}$  (all units in  $\text{W m}^{-2}$ ) from RAMA buoy observations (a, b, c, d), ERA-I (e, f, g, h), TropFlux (i, j, k, l), JRA-55 (m, n, o, p), MERRA-2 (q, r, s, t) and CFSR (u, v, w, x) at site b28 (8°N and 90°E). Contour lines enclose the 10% and 50% of points in each joint distribution. RAMA contour lines (black) are repeated for comparison.

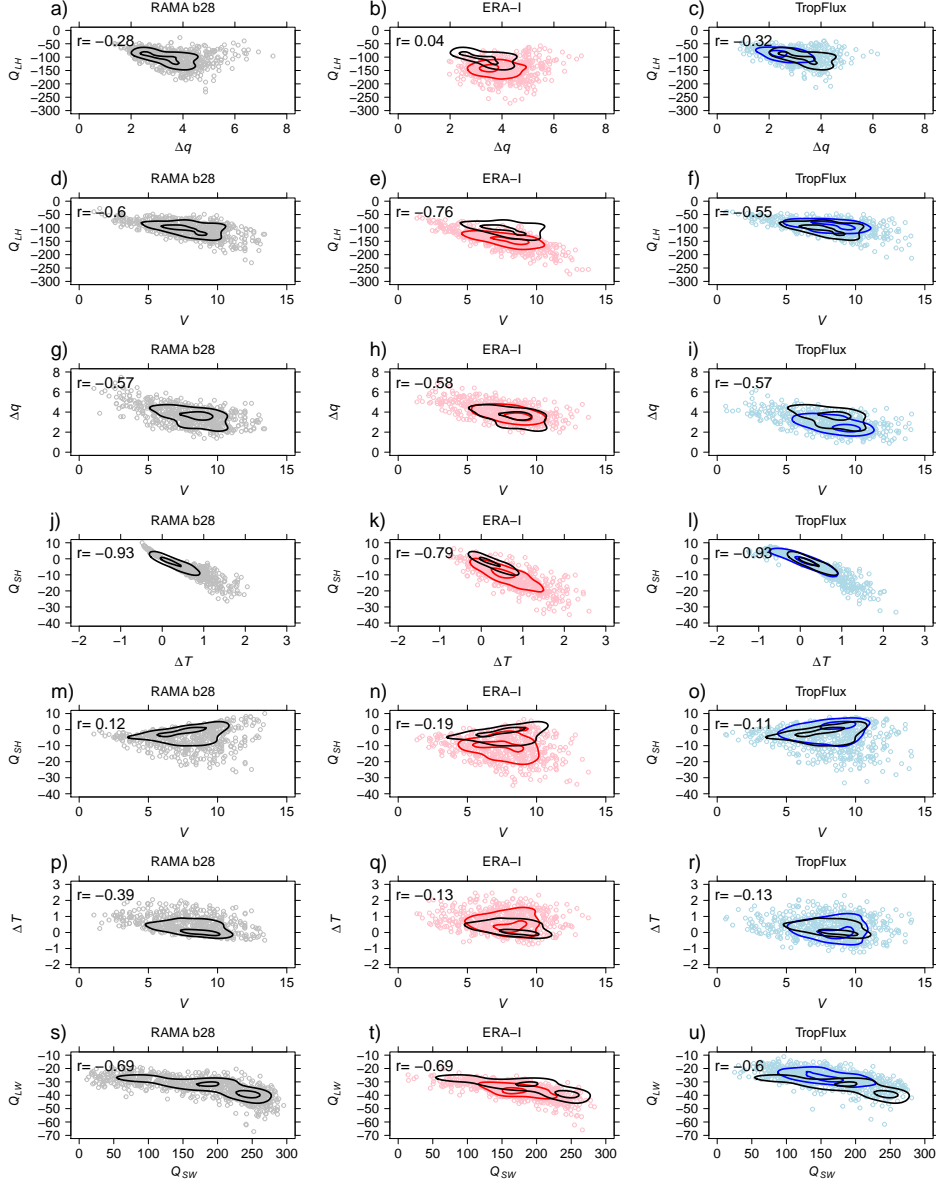


FIG. 4. Scatterplots of  $Q_{LH}$  (W m<sup>-2</sup>) vs  $\Delta q$  (g kg<sup>-1</sup>),  $Q_{LH}$  (W m<sup>-2</sup>) vs  $V$  (m s<sup>-1</sup>),  $Q_{SH}$  (W m<sup>-2</sup>) vs  $\Delta T$  (°C),  $Q_{SH}$  (W m<sup>-2</sup>) vs  $V$  (m s<sup>-1</sup>),  $\Delta T$  (°C) vs  $V$  (m s<sup>-1</sup>), and  $Q_{LW}$  (W m<sup>-2</sup>) vs  $Q_{SW}$  (W m<sup>-2</sup>) from RAMA buoy observations (left column), ERA-Interim (center column) and TropFlux (right column) at site b28 (8°N and 90°E). Contour lines enclose the 10% and 50% of points in each joint distribution. RAMA contour lines (black) are repeated for comparison.



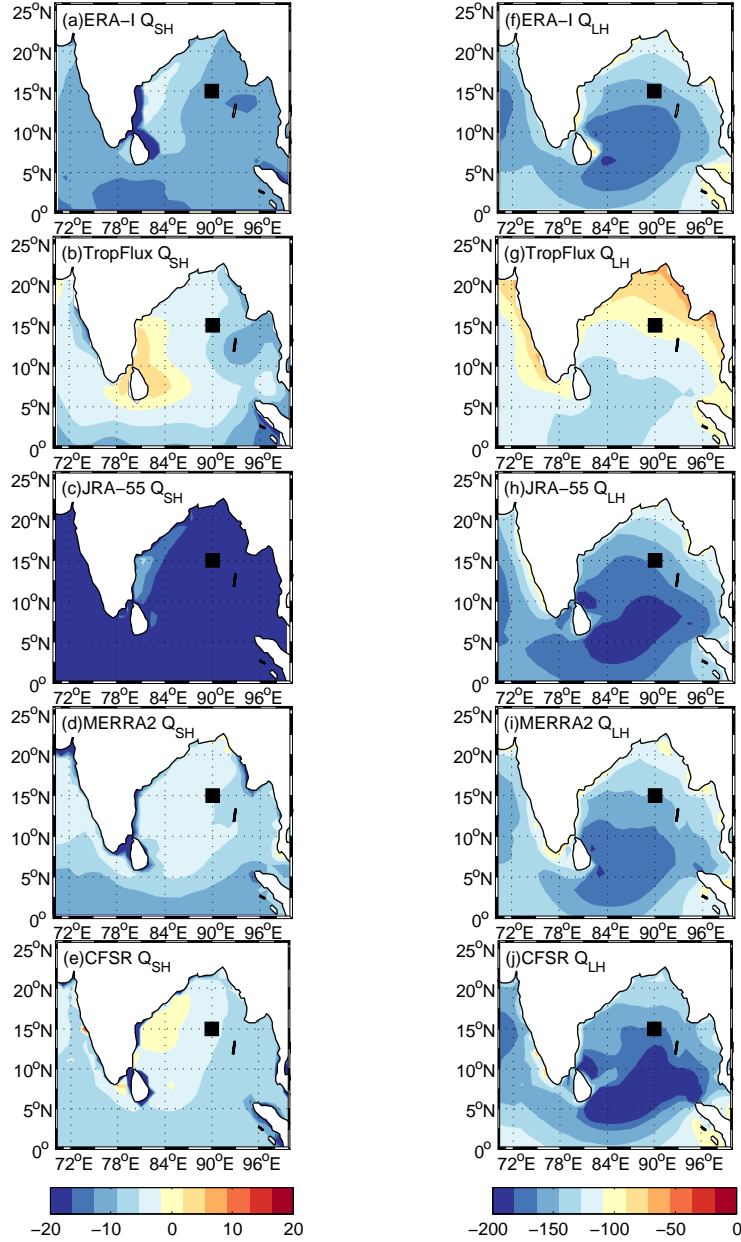


FIG. 5. Mean  $Q_{SH}$  (left column;  $W m^{-2}$ ) and  $Q_{LH}$  (right column;  $W m^{-2}$ ) for ERA-I (a, f), TropFlux (b, g), JRA-55 (c, h), MERRA-2 (d, i), and CFSR (e, j). All fields are averaged for the SW monsoon season (JJAS) from 2007 to 2015. The black square indicates the location of the RAMA buoy, b28, in the Bay of Bengal.

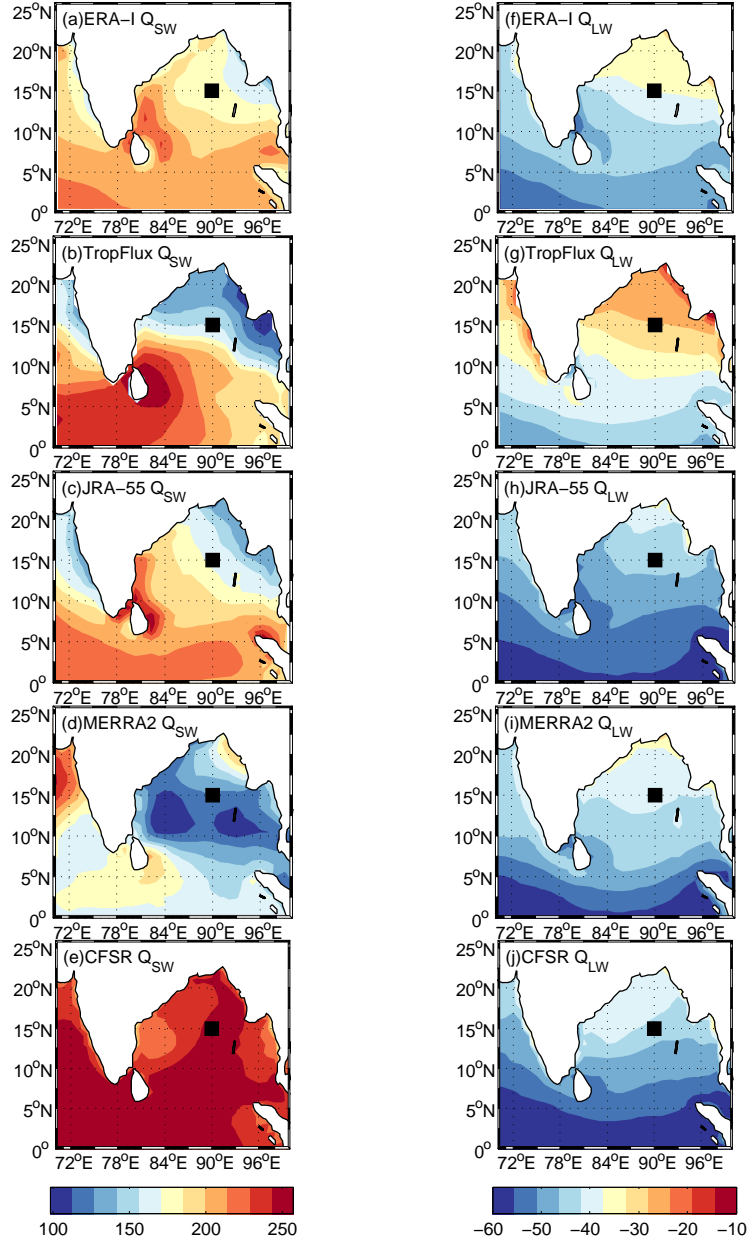


FIG. 6. Same as in Fig. 5 but for radiative fluxes.

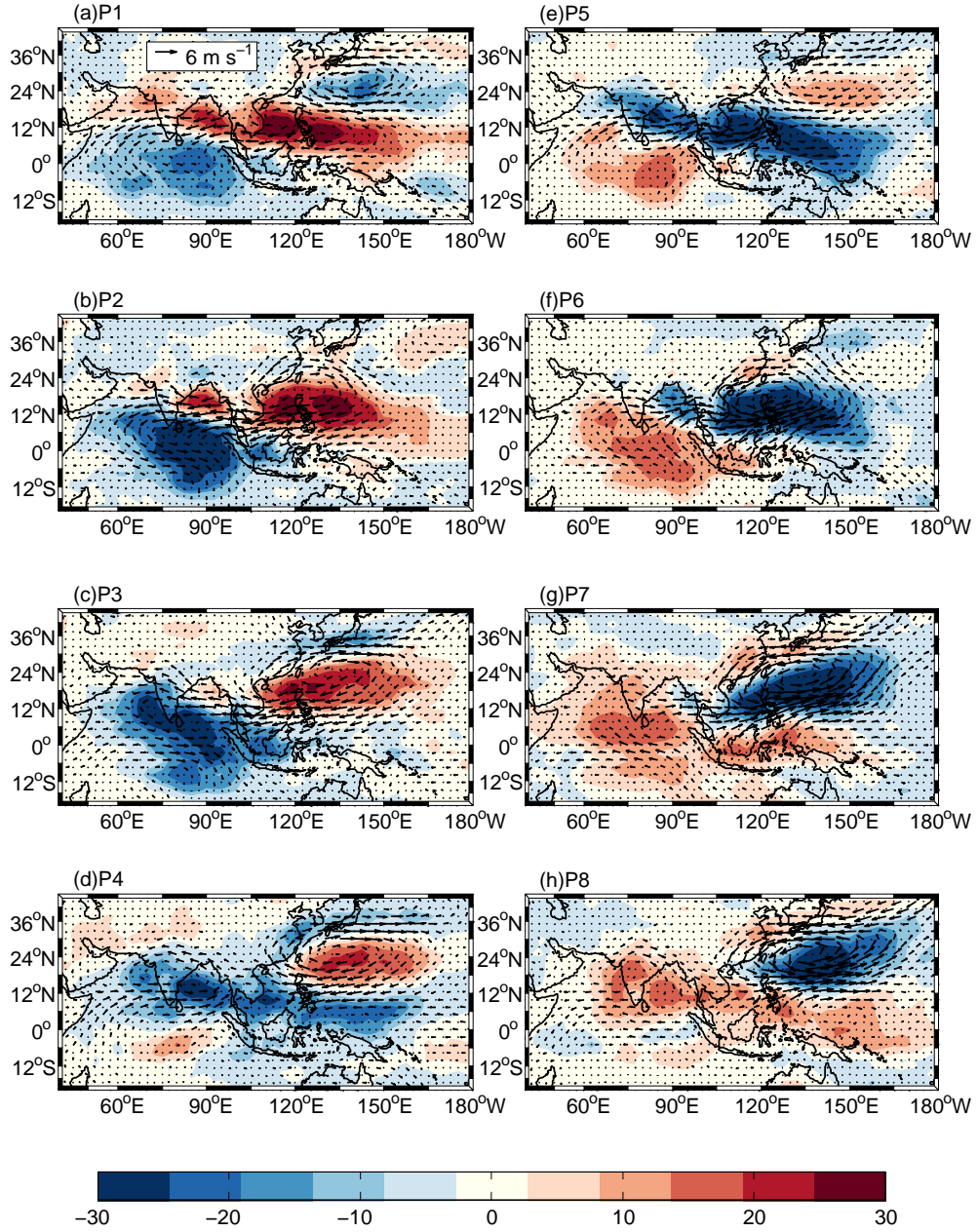


FIG. 7. BISO 1 life cycle composite of NOAA OLR anomalies (shaded;  $\text{W m}^{-2}$ ) and NCEP-DOE 850-hPa wind anomalies (vector;  $\text{m s}^{-1}$ ).

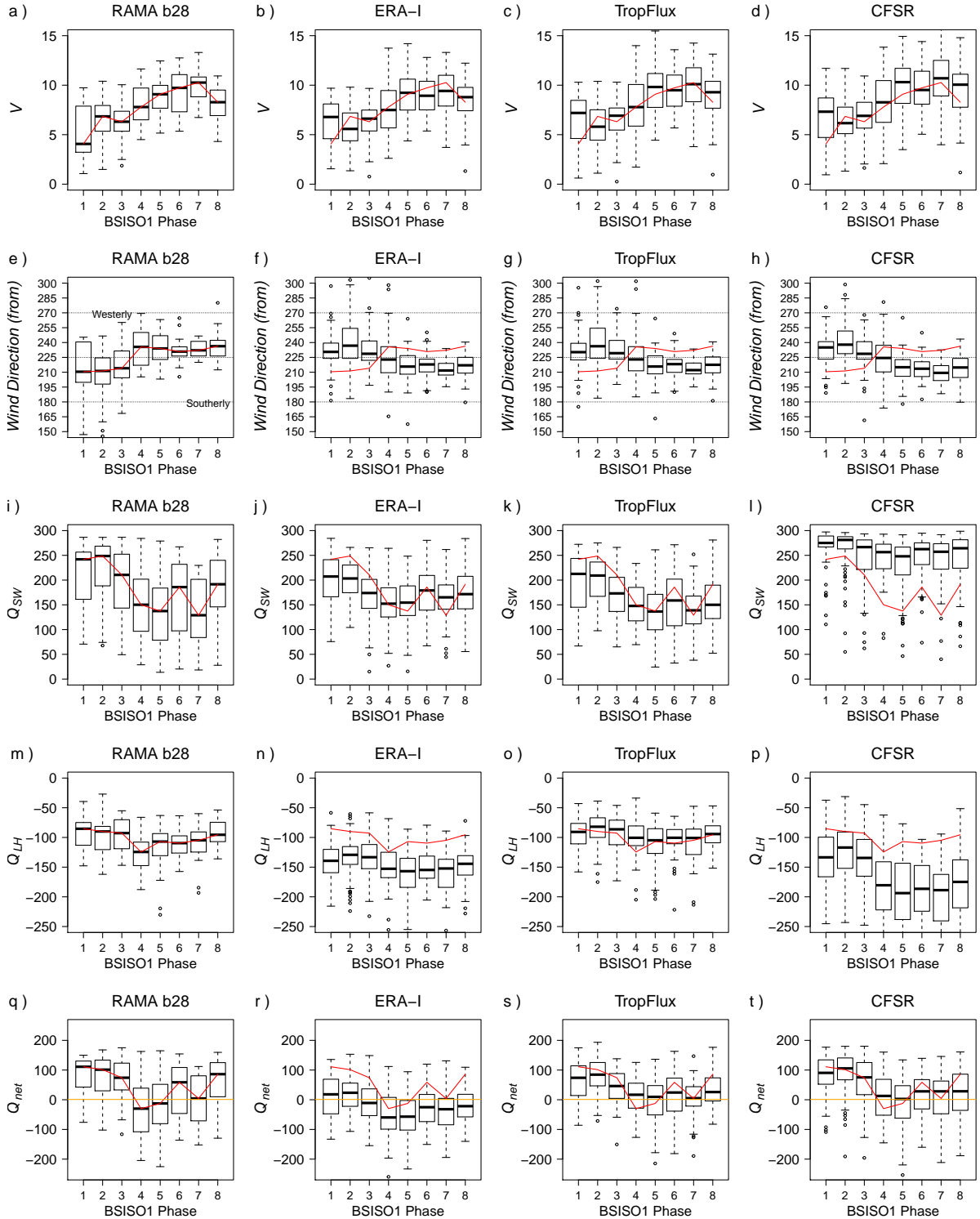


FIG. 8. Median, interquartile range, 95% confidence interval, and outliers for  $V$  (m s<sup>-1</sup>), wind direction (°),  $Q_{SW}$  (W m<sup>-2</sup>),  $Q_{LH}$  (W m<sup>-2</sup>), and  $Q_{net}$  (W m<sup>-2</sup>) vs BSISO1 phases (1 to 8) from RAMA b28 (a, e, i, m, q), ERA-I (b, f, j, n, r), TropFlux (c, g, k, o, s), and CFSR (d, h, l, p, t). The red line is the RAMA b28 median line, repeated for comparison.

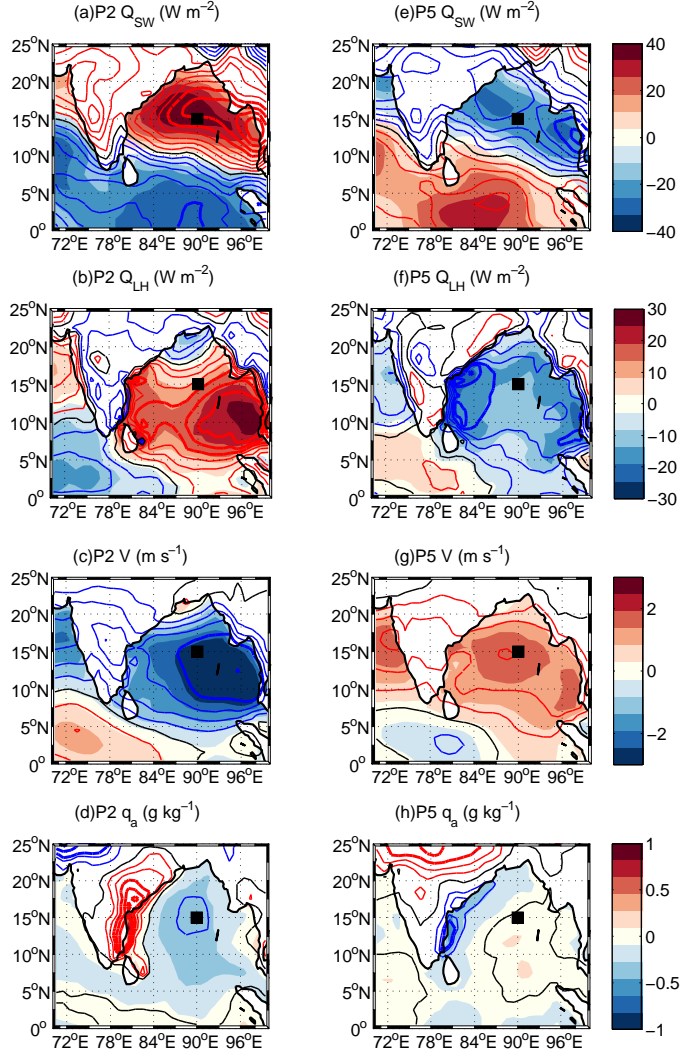


FIG. 9. Composite of phase 2 (left column) and phase 5 (right column) of the BSISO1 life cycle. TropFlux (shaded) and ERA-I (contour lines)  $Q_{SW}$  anomalies at phase 2 (a) and phase 5 (e);  $Q_{LH}$  anomalies at phase 2 (b) and 5 (f);  $V$  anomalies at phase 2 (c) and 5 (g); and,  $q_a$  anomalies at phase 2 (d) and 5 (h). ERA-I  $Q_{SW}$  contour lines range from -40 to 40  $W m^{-2}$  and  $Q_{LH}$  contour lines range from -30 to 30  $W m^{-2}$ , with 5  $W m^{-2}$  intervals. ERA-I  $V$  contour lines range from -3 to 3  $m s^{-1}$ , with 0.5  $m s^{-1}$  intervals. ERA-I  $q_a$  contour lines range from -1 to 1  $g kg^{-1}$ , with 0.2  $g kg^{-1}$  intervals. The black square indicates the location of the RAMA buoy 28.

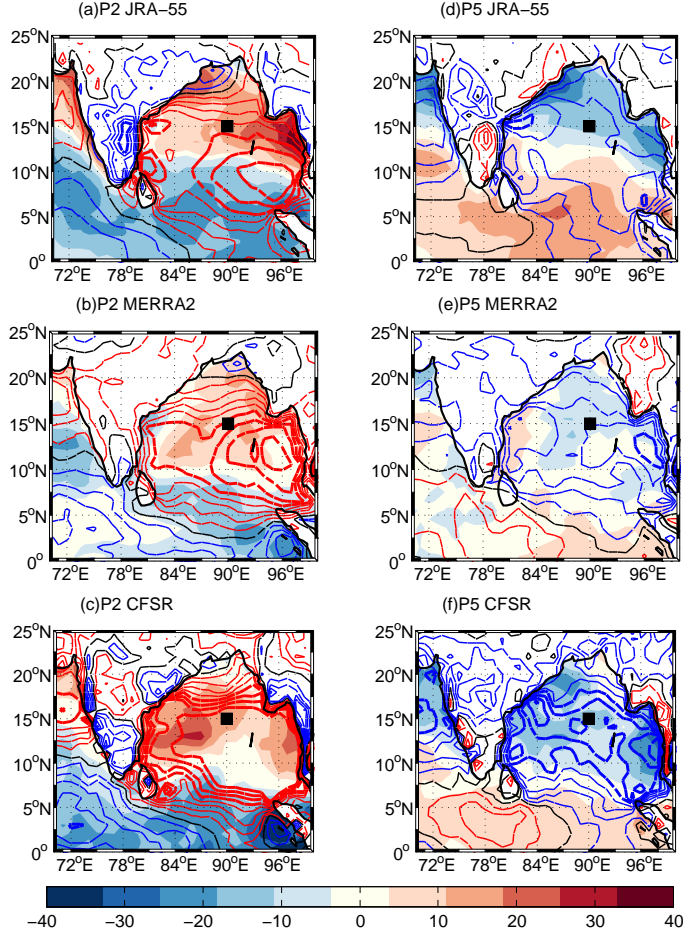


FIG. 10. Phase 2 (left column) and 5 (right column) of the  $Q_{SW}$  (shading) and  $Q_{LH}$  (contour line) anomalies from JRA-55 (a, d), MERRA-2 (b, e), and CFSR (c, f) based on the BSISO1 phases.  $Q_{LH}$  contour lines range from -40 to 40  $W m^{-2}$ , with 5  $W m^{-2}$  intervals. The black square indicates the location of the RAMA buoy 28. All units in  $W m^{-2}$ .